Modal and nonmodal stability of a stably stratified boundary layer flow

E. Parente,[1,2] J. C. Robinet [ORCID],[1] P. De Palma,[2] and S. Cherubini[2,*]

[1]*Laboratoire DynFluid, Arts et Métiers ParisTech, 151 Bd. de l'Hopital, 75013 Paris, France*
[2]*Dipartimento di Meccanica, Matematica e Management, Politecnico di Bari,*
Via Re David 200, 70125 Bari, Italy

The modal and nonmodal linear stability of a stably stratified Blasius boundary layer flow, composed of a velocity and a thermal boundary layer, is investigated. The temporal and spatial linear stability of such flow is investigated for several Richardson, Reynolds, and Prandtl numbers. While increasing the Richardson number stabilizes the flow, a more complex behavior is found when changing the Prandtl number, leading to a stabilization of the flow up to $Pr = 7$, followed by a destabilization. The nonmodal linear stability of the same flow is then investigated using a direct-adjoint procedure optimizing four different approximations of the energy norm based on a weighted sum of the kinetic and the potential energies. No matter the norm approximation, for short target times an increase of the Richardson number induces a decrease of the optimal energy gain and time at which it is obtained and an increase of the optimal streamwise wave number, which considerably departs from zero. Moreover, the dependence of the energy growth on the Reynolds number transitions from quadratic to linear, whereas the optimal time, which varies linearly with Re in the nonstratified case, remains constant. This suggests that the optimal energy growth mechanism arises from the joint effect of the lift-up and the Orr mechanism, that simultaneously act to increase the shear production term on a rather short timescale, counterbalancing the stabilizing effect of the buoyancy production term. Although these short-time mechanisms are found to be robust with respect to the chosen norm, a different amplification mechanism is observed for long target times for three of the proposed norms. This strong energy growth, due to the coupling between velocity and temperature perturbations in the free stream, disappears when the variation of the stratification strength with height is accurately taken into account in the definition of the norm.

I. INTRODUCTION

Stratified shear flows occur in many hydrodynamical, industrial, and geophysical applications, some common examples being atmospheric boundary layers and oceans, volcanic plumes, under-ice convection, chimney exhausts, saline jets, and lifted flames. All these flows are characterized by a variation of density along a cross-stream direction, which can be modeled by a buoyancy force in the momentum equations. This buoyancy effect can be generated as a consequence of low-density fluid injected into a high-density fluid, or due to a phase change or chemical reactions, or, as in oceans, it can be originated by the presence of salinity and traces of carbon and nutrients. When the buoyancy forces overcome the dissipative ones due to thermal and viscous diffusion, these flows may become linearly unstable by means of a mechanism similar to that triggering natural convection

---

*s.cherubini@gmail.com

cells in a stationary fluid layer heated from below. A typical example of such a linear instability is the formation of cloud streets in the atmospheric boundary layer, characterized by convection rolls aligned with the direction of the flow [1]. This peculiar fluid motion is commonly encountered in geophysical flows, but also in industrial ones such as heat exchangers, provided that the flow is characterized by an *unstable* stratification, i.e., that the buoyancy force is directed opposed to temperature gradient. The hydrodynamic instability arising in these conditions is characterized by the asymptotic growth of wavelike perturbations on the steady laminar base flow, which exponentially grow, eventually leading the laminar flow to a turbulent state. Gage and Raid [2] were among the first to study the linear stability of a thermally stratified shear fluid, in which the instability arises from interaction between the convection mechanisms due to thermal stratification and the Tollmien-Schlichting mechanism due to the shear.

In the inviscid limit, it is known that a parallel shear flow remains asymptotically stable to small-amplitude disturbances when the gradient Richardson number Ri_g is larger than 0.25; whereas, for Ri_g below this value, asymptotic modal instability may occur. In the case of viscous flow with unstable stratification, there is an abrupt transition between the thermal mode, which sets in at a certain value of the Rayleigh number, independently of the shear, and the Tollmien-Schlichting mode, which appears at high shear rates. This transition occurs at a small negative value of the Richardson number, and for Ri lower than this threshold, Squire's theorem is no longer valid.

The influence of buoyancy on nonmodal stability, such as on the transient energy growth phenomenon which arises as a consequence of the non-normality of the Navier-Stokes operator, has been investigated in several parallel shear flows. In the presence of unstable stratification [3], the optimal energy growth of plane Couette and Poiseuille flows increases slowly with the Prandtl and Rayleigh numbers, although its maximum value is always attained for streamwise-homogeneous perturbations which produce large streamwise streaks and Rayleigh-Bénard convection rolls. In the short-time limit, the amplification is governed by the classical lift-up mechanism, with a negligible influence of buoyancy. Whereas, in the long-time limit, as anticipated for an asymptotically unstable flow, the optimal perturbation is given by the adjoint of the dominant eigenmode.

Many studies have been conducted to investigate the effect of stable stratification on the linear stability of classical parallel shear flows. For instance, in Ref. [4], a plane Couette flow stably stratified in the wall-normal direction is considered. The flow becomes asymptotically unstable when shear and stratification become of the same order and for sufficiently high values of the Reynolds number (Re > 700). The result is confirmed by nonlinear direct numerical simulations and experiments providing an evidence of the development of linear modal instabilities in a vertically stably stratified plane Couette flow. Biau and Bottaro [5] studied the effect of buoyancy on the stability of a plane Poiseuille flow in the presence of a constant positive thermal gradient. By means of linear stability analyses in the modal and nonmodal frameworks, they found that positive thermal stratification is found to stabilize the shear flow, marginally affecting the shape and main features of the unstable modes and optimal disturbances. A similar flow case has been considered in Ref. [6], although the transient growth optimizations were performed with a different norm and the case of unstable stratification was considered as well. It was found that, increasing the Prandtl number to values of order 1, causes a growth of disturbances of one order of magnitude higher with respect to the unstratified case, giving rise to spanwise-independent optimal perturbations, instead of streamwise vortices found at Pr = 0. Linear transient-growth analysis around the mean velocity and density flow profiles in a stably- tratified turbulent channel showed that the perturbations experiencing the optimal transient growth consists of spanwise stripes, confined within the core region [7]. Remarkably, similar homogeneous spanwise stripes have been also found [8] by direct numerical simulation at the center of a turbulent stably stratified channel, suggesting that the dynamics of the stably stratified turbulent flows is considerably different from that of nonstratified ones, and that nonmodal stability analysis may succeed at characterizing them. More recently, studies have been conducted to investigate the effect of buoyancy in destabilizing the flow fields of buoyant jets and plumes in a laminar setting before they undergo transition to turbulence. The local [9] and global [10] stability analysis of a helium jet injected vertically into quiescent air is

considered and the interaction between the inertia force imparted at the inlet and the buoyancy force due to the low density of the helium injected in the air is investigated varying the Richardson number.

The role of stable stratification on the Kelvin-Helmholtz instability that can be triggered in mixing layers such as those encountered in the ocean [11] has been recently investigated by linear optimization procedures [12,13]. For short target times, the optimal perturbations are three dimensional, while for long target times and small values of the Richardson number, they are related to Kelvin-Helmholtz instability, consistent with analogous calculations in an unstratified mixing layer. Large transient growth occurs even when the Richardson number is sufficiently high to stabilize all modal instabilities, linked to the onset of internal waves at some distance from the shear layer.

Apart from the classical parallel flows such as shear layers, Couette and channel flows, a stratified flow of wide-ranging practical interest is the boundary layer flow. The characterization of the dynamics of stratified boundary layer flows is of fundamental importance nowadays, being the development of large-scale coherent structures in atmospheric boundary layer flows intrinsically inherent in weather prediction, climate-change assessment, as well as in the modeling of turbine wakes in wind farms. Early investigations of the stability of such flows considered mean profiles corresponding to certain atmospheric conditions (see [14], among others). Restricting the analysis to the inviscid limit, they found linearly unstable Kelvin-Helmholtz (KH) type modes with wavelengths comparable with the width of the background shear layer, localized in correspondence with the critical layer, i.e., the region where the base-flow velocity equals the phase speed. However, instability waves are often observed in atmospheric boundary layers whose velocity profiles are devoid of an inflection point, which are expected to be stable to inviscid instabilities [15]. The stability of an inflection-free compressible stratified boundary layer flow [16] was investigated in the inviscid limit, establishing that this flow becomes unstable with respect to inviscid perturbations when the boundary surface is inclined with respect to the isodensity levels. The first study tackling viscous modal instabilities in a stably stratified boundary layer [17] made use of the triple-deck theory in a spatial and temporal formulation, showing that stable stratification may increase the growth of *temporal* instabilities. In Ref. [18] the modal stability of a stably stratified boundary layer flow on a vertical wall is studied, taking into account viscous effects. Even in the presence of stratification, the most unstable mode is a Tollmien-Schlichting wave, which remains two dimensional and independent of the Froude number. A radiative instability is observed as well, which is three dimensional, inviscid, and associated with buoyancy effects. Although these studies have unveiled the asymptotic behavior of stratified boundary layer flows with respect to small-amplitude wavelike perturbations, it is known that, at moderate Reynolds numbers, the boundary layer is extremely sensitive to external noisy perturbations, which can transiently grow, leading to turbulent transition bypassing the asymptotic growth of wavelike modes [19]. The knowledge of these transient growth mechanisms is fundamental for an accurate modeling of the flow. In fact, the onset of turbulence and the resulting mixing strongly affect key processes such as atmospheric and oceanic circulation processes which have a strong impact on weather and climate. How the transient energy growth mechanisms often observed in shear flows are influenced by stable stratification and compete with the asymptotic instability remains an interesting issue which is at the moment still open. Moreover, in the case of a stratified flow consisting of a thermal and a velocity boundary layer, nonmodal stability analysis is not straightforward from a methodological point of view, due to the nonobvious choice of an appropriate norm which should correctly take into account the contribution of the potential energy. As discussed by many authors in the past [20–22], a correct and positive-definite expression of the potential energy of small-amplitude perturbations to a stratified base flow should take into account the variation of the stratification strength with height. To model this effect, the potential energy is usually characterized by a height-dependent Brunt-Väisälä frequency in the denominator. In the case of a thermal boundary layer, the Brunt-Väisälä frequency is null in the free-stream region, inducing a peculiar divergent behavior of the energy in that particular region. This makes the choice of a meaningful norm to optimize an interesting problem per se in the case of thermal boundary layers.

In this work, we investigate the modal and nonmodal instabilities of a Blasius boundary layer flow with stable stratification due to the presence of a thermal boundary layer, whose thickness is linked to that of the velocity profile by the Prandtl number. Considering this model flow is a first attempt toward the investigation of the stability of the complex case of the stably stratified atmospheric boundary layer, characterized by a higher positive thermal gradient near the ground that decreases toward neutral conditions with height, as in night-time conditions, when the radiative cooling makes the near-the-surface air cooler than the air above. Although atmospheric boundary layers are often turbulent, in nocturnal conditions they remain most of the time in a laminar state, interrupted by short outbursts of intermittent turbulence [23], making our approach appropriate for qualitatively characterizing the waves that develop and amplify over the laminar state, probably being at the origin of such turbulent bursts. In such a laminar base flow, modal and nonmodal stability analyses are carried out for different values of the Richardson, the Prandtl, and the Reynolds numbers, in order to unveil how buoyancy affects the stability of the flow. Nonmodal stability analysis is performed with respect to four different approximations of the energy norm, taking into account or not the variation of the stratification strength with height. The instability and energy growth mechanisms are identified and discussed by analyzing the evolution of the different production terms in the equations governing the energy exchange.

The paper is organized as follows. In Sec. II, we present the problem formulation and describe the base flow and the modal and nonmodal stability frameworks. In Sec. III A we present the results of the modal stability analysis, whereas those related to the nonmodal stability approach are presented in Secs. III B 1 and III B 2 in the case of short [$O(10)$] and long [$O(10^3)$] timescales, respectively. Conclusions are provided in Sec. IV.

II. PROBLEM FORMULATION

The dynamics of an incompressible boundary layer flow in the presence of temperature stratification in the wall-normal direction can be described by the Navier-Stokes (NS) equations with the Boussinesq approximation:

$$\boldsymbol{\nabla} \cdot \check{\mathbf{U}}_b = 0, \tag{1}$$

$$\check{\rho}_0 \frac{\partial \check{\mathbf{U}}_b}{\partial \check{t}} + \check{\rho}_0 (\check{\mathbf{U}}_b \cdot \boldsymbol{\nabla}) \check{\mathbf{U}}_b = -\boldsymbol{\nabla} \check{P}_b + \check{\mu} \nabla^2 \check{\mathbf{U}}_b - \check{\rho}_b \check{g} \mathbf{e}_y, \tag{2}$$

$$\frac{\partial \check{T}_b}{\partial \check{t}} + (\check{\mathbf{U}}_b \cdot \boldsymbol{\nabla}) \check{T}_b = \check{\kappa} \nabla^2 \check{T}_b, \tag{3}$$

$$\check{\rho}_b = \check{\rho}_0 [1 - \check{\alpha}_T (\check{T}_b - \check{T}_0)], \tag{4}$$

where $\check{\mathbf{U}}_b = (\check{U}_b, \check{V}_b, \check{W}_b)^T$ is the velocity vector, $\check{T}_b$ is the temperature, $\check{\mu}$ the dynamic viscosity, $\check{\rho}_b$ and $\check{p}_b$ represent the density and the pressure, respectively, $\check{g}$ is the gravitational acceleration acting along the wall-normal direction $\check{y}$, represented by the unit vector $\mathbf{e}_y$, $\check{\kappa}$ is the thermal diffusivity coefficient, $\check{\rho}_0$ and $\check{T}_0$ are the standard density and temperature, respectively, $\check{\alpha}_T$ is the thermal expansion coefficient, and the $\check{}$ symbol indicates dimensional quantities.

Nondimensional quantities are obtained with respect to the free-stream velocity $\check{U}_\infty$, the displacement thickness of the boundary layer $\check{\delta}_v^*$, and the temperature variation $\Delta \check{T}_b$ between the free stream and the wall (see the sketch in Fig. 1). Throughout the paper, variables with the superscript $\check{}$ are dimensional, whereas nondimensional ones are those without superscripts.

Let us now consider a steady solution $\mathbf{Q}_b = (\mathbf{U}_b, P_b, T_b)$ of the NS equations (1)–(3) (i.e., with all time derivatives set to zero), and a perturbation of this base state, $\mathbf{q} = (\mathbf{u}, p, T)$, where $\mathbf{u} = (u, v, w)^T$ is the perturbation velocity vector, T is the temperature disturbance, and p represents the pressure disturbance. Being interested in the behavior of infinitesimal three-
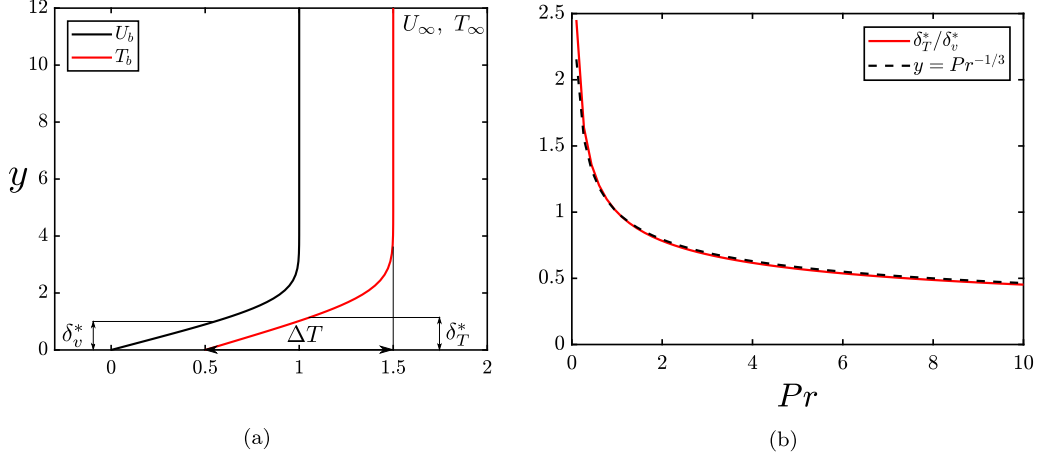
FIG. 1. Stratified Blasius base-flow sketch. (a) Streamwise velocity and temperature profiles of the analytical Blasius solution with Pr = 0.7. (b) Ratio between the temperature and the velocity boundary layer thicknesses versus the Prandtl number.

dimensional perturbations, we write the nondimensional perturbative linearized NS equations as follows:

$$\nabla \cdot \mathbf{u} = 0, \tag{5}$$

$$\frac{\partial \mathbf{u}}{\partial t} + (\mathbf{u} \cdot \nabla)\mathbf{U}_b + (\mathbf{U}_b \cdot \nabla)\mathbf{u} = -\nabla p + \frac{1}{\text{Re}}\nabla^2 \mathbf{u} + \text{Ri}T\mathbf{e}_y, \tag{6}$$

$$\frac{\partial T}{\partial t} + (\mathbf{u} \cdot \nabla)T_b + (\mathbf{U}_b \cdot \nabla)T = \frac{1}{\text{Re Pr}}\nabla^2 T, \tag{7}$$

where $\text{Re} = \check{U}_\infty \check{\delta}_v^* / \check{v}$ is the Reynolds number, $\text{Pr} = \check{\mu}/(\check{\rho}\check{\kappa}) = \check{v}/\check{\kappa}$ the Prandtl number, defined as the ratio of momentum diffusivity to thermal diffusivity, and Ri is the bulk Richardson number, representing the ratio of the buoyancy effect to the flow shear one, defined as follows:

$$\text{Ri} = \frac{\check{\alpha}_T \check{g}\Delta\check{T}_b\check{\delta}_v^*}{\check{U}_\infty^2}. \tag{8}$$

Since we are interested in weakly or moderately stratified boundary layer flows, we use rather low values of the Richardson number ($\text{Ri} \leqslant 10^{-1}$), and Prandtl numbers ranging from 10^{-2} to 100 (where Pr = 0.7 corresponds to air and Pr = 7 to water).

A. Stratified Blasius flow

To carry out a *local stability analysis*, it is necessary to define a base flow homogeneous along the streamwise (x) and the spanwise (z) directions, such as

$$\mathbf{U}_b = (U_b(y), 0, 0)^T, \quad T_b = T_b(y), \tag{9}$$

where $U_b(y)$ and $T_b(y)$ are the velocity and thermal boundary layers developing in a fluid flowing over an isothermal surface having a different temperature with respect to the free-stream one. The velocity and thermal boundary layer profiles are found as solutions of the Blasius system of ordinary differential equations:

$$f'''(\eta) + \tfrac{1}{2}f(\eta)f''(\eta) = 0, \quad \theta''(\eta) + \tfrac{1}{2}\text{Pr}f(\eta)\theta'(\eta) = 0, \tag{10}$$

where the prime indicates differentiation with respect to $\eta = y/\delta(x)$, δ being the boundary layer thickness, $f(\eta)$ is the normalized stream function, $\theta(\eta)$ is the normalized temperature function. To ensure a stable stratification the following boundary conditions are imposed:

$$f(0) = f'(0) = 0, \quad f(\infty) = 1, \quad \theta(0) = 0, \quad \theta(\infty) = 1. \tag{11}$$

The velocity and the temperature of the base flow are reconstructed in the following way:

$$U_b(y) = f'(\eta), \quad T_b(y) = T_\infty - \theta(\eta), \tag{12}$$

where T_∞ is the nondimensional free-stream temperature. Figure 1 reports the velocity and temperature base-flow profiles for the stratified Blasius flow with $\mathrm{Pr} = 0.7$ (left frame) as well as the variation of the ratio between the velocity displacement thickness and the temperature one with respect to the Prandtl number (right frame). The ratio of the displacement thicknesses of the velocity and thermal boundary layers depends on the Prandtl number [24] as follows:

$$\frac{\check{\delta}_T^*}{\check{\delta}_v^*} = \mathrm{Pr}^{-\frac{1}{3}}. \tag{13}$$

When $\mathrm{Pr} < 1$ (for instance, $\mathrm{Pr} = 0.7$ for air at standard conditions), the thermal boundary layer is thicker than the velocity boundary layer, whereas when $\mathrm{Pr} > 1$, the thermal boundary layer is thinner than the velocity boundary layer.

B. Modal stability analysis

Modal stability analysis in a local framework implies searching for solutions of the linearized system (5)–(7) of the following form:

$$\mathbf{q}(\mathbf{x}, t) = \hat{\mathbf{q}}(y)e^{i(\alpha x + \beta z - \omega t)} + \mathrm{c.c.}, \tag{14}$$

where $\hat{\mathbf{q}}$ is the Fourier-Laplace transform of $\mathbf{q}(\mathbf{x}, t) = (\mathbf{u}, p, T)(\mathbf{x}, t)$, c.c. is its complex conjugate, ω is the complex pulsation, and α, β are the wave numbers in the x, z directions, respectively. Replacing the base-flow profiles (12) and the fluctuation form (14) in the linearized system (5)–(7), the following equations are obtained:

$$i\alpha\hat{u} + \frac{d\hat{v}}{dy} + i\beta\hat{w} = 0, \tag{15}$$

$$i(\alpha U_b - \omega)\hat{u} + \hat{v}\frac{dU_b}{dy} + = -i\alpha\hat{p} + \frac{1}{\mathrm{Re}}\left(\frac{d^2\hat{u}}{dy^2} - (\alpha^2 + \beta^2)\hat{u}\right), \tag{16}$$

$$i(\alpha U_b - \omega)\hat{v} = -\frac{d\hat{p}}{dy} + \frac{1}{\mathrm{Re}}\left(\frac{d^2\hat{v}}{dy^2} - (\alpha^2 + \beta^2)\hat{v}\right) + \mathrm{Ri}\hat{T}, \tag{17}$$

$$i(\alpha U_b - \omega)\hat{w} + = -i\beta\hat{p} + \frac{1}{\mathrm{Re}}\left(\frac{d^2\hat{w}}{dy^2} - (\alpha^2 + \beta^2)\hat{w}\right), \tag{18}$$

$$i(\alpha U_b - \omega)\hat{T} + \hat{v}\frac{dT_b}{dy} = \frac{1}{\mathrm{Re}\,\mathrm{Pr}}\left(\frac{d^2\hat{T}}{dy^2} - (\alpha^2 + \beta^2)\hat{T}\right). \tag{19}$$

These equations are completed by the following boundary conditions:

$$\hat{u} = \hat{v} = \hat{w} = \hat{T} = 0, \tag{20}$$

at the wall and at the far-field boundary. The stability problem thus assumes the following matrix formulation:

$$\mathcal{L}(\alpha, \beta, \omega, \mathbf{U}_b, T_b)\hat{\mathbf{q}}(\mathbf{x}, \alpha, \beta, \omega) = \mathbf{0}, \tag{21}$$

where $\hat{\mathbf{q}} = (\hat{u}, \hat{v}, \hat{w}, \hat{p}, \hat{T})$ and $\mathcal{L}$ is the linear operator of the eigenvalue problem that can be solved using a temporal or spatial approach. In this work the spatial problem, which consists of the analysis

of the base-state response to time-harmonic forcing with real frequency ω and complex streamwise wave number α, is solved as

$$[\mathcal{C}_2\alpha^2 + \mathcal{C}_1\alpha + \mathcal{C}_0]\hat{\mathbf{q}}(\mathbf{x}; \alpha, \beta, \omega) = \mathbf{0} \tag{22}$$

to find α for given values of ω and β. If the imaginary part of α is greater than zero, the flow is defined as spatially stable.

To solve the spatial stability problems defined above, we discretize the derivative operators using a spectral collocation method in order to build the Jacobian matrix of the linearized system. Spatial discretization in the wall-normal direction is accomplished using Chebyshev polynomials on the Gauss-Lobatto points. A conformal mapping is then used to transform the Chebyshev interval in the physical domain $y \in [0, y_{\max}]$, using $N_y = 100$ grid points. The boundary conditions given in Eq. (20) are imposed in an implicit way. The resulting discrete counterpart of Eq. (22) is solved using MATLAB. The obtained eigenvalues and eigenvectors have been validated with respect to the case of the (unstratified) Blasius flow, as well as with the stratified channel flow computed in Ref. [5], finding a very good agreement.

C. Nonmodal stability analysis

Nonmodal stability analysis focuses on the finite-time behavior of small-amplitude disturbances, which may experience transient energy growth due to the non-normality of the linear operator $\mathcal{L}$ [see Eq. (21)]. This problem results in an optimization of an appropriate energy norm, aiming at finding the initial condition allowing for the maximum growth of the chosen energy at a given time $\bar{t}$. When dealing with unstratified shear flows, the chosen energy norm to be optimized is usually the kinetic energy of the perturbation [25] although other norms [26] or seminorms [27,28] have been also used in the literature. For stratified flows, the appropriate norm may include the potential energy term. Therefore, in the case of small-amplitude perturbations and using the Boussinesq approximation, the global energy norm to be optimized reads as [20,21]

$$\check{E}(t) = \int_V (\check{e}_K + \check{e}_P)dV = \int_V \left(\frac{\check{\rho}_0}{2}|\check{\mathbf{u}}(\mathbf{x}, t)|^2 - \frac{\check{g}}{2\check{\rho}_b'}\check{\rho}^2(\mathbf{x}, t) \right)dV, \tag{23}$$

where the prime indicates the derivative with respect to the y direction, V is the volume of the computational domain, $\check{e}_K$ and $\check{e}_P$ indicate the local kinetic and potential energies of the perturbation, respectively. Using Eq. (4), the following expression is obtained,

$$\check{E}(t) = \frac{1}{2} \int_V \left(\check{\rho}_0|\check{\mathbf{u}}(\mathbf{x}, t)|^2 + \frac{\check{g}\check{\rho}_0\check{\alpha}_T}{\check{T}_b'}\check{T}^2(\mathbf{x}, t) \right)dV. \tag{24}$$

Finally, reverting to nondimensional variables, one has

$$E(t) = \frac{1}{2} \int_V [|\mathbf{u}(\mathbf{x}, t)|^2 + \phi(y)T^2(\mathbf{x}, t)]dV, \tag{25}$$

where

$$\phi(y) = \mathrm{Ri}/T_b'(y). \tag{26}$$

Previous works have employed for transient growth analysis a formulation of the global energy of a similar form with the coefficient ϕ equal to a constant. For instance, in Ref. [3], the nonmodal stability of plane Poiseuille and Couette flows with constant temperature gradient, solution of the Oberbeck-Boussinesq equations, are studied using an equivalent of the previously defined norm with $\phi = \mathrm{Ra}_{\mathrm{bulk}}\mathrm{Pr}$, where $\mathrm{Ra}_{\mathrm{bulk}}$ is the bulk Rayleigh number. In Ref. [5], the transient energy growth of the stratified plane Poiseuille base flow with constant temperature gradient has been studied using the norm (25) with constant value of $\phi = 2\,\mathrm{Ri}/T_b'$ and scaling the spanwise, and wall-normal kinetic energy contributions with the inverse of Re^2. In Ref. [6], the nonmodal stability of the stratified plane Poiseuille flow has been studied by analyzing only the behavior of the kinetic energy of
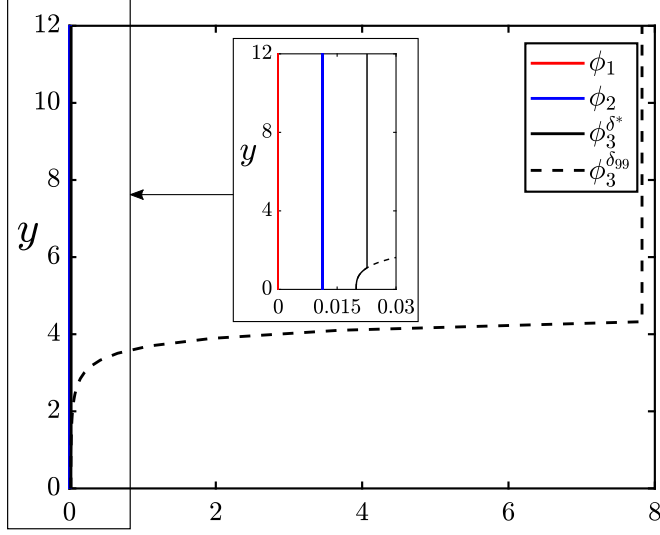
FIG. 2. Values of $\phi(y)$ for the different approximations of the energy norm.

the perturbation ($\phi = 0$) or considering $\phi = 2$. It is noteworthy that the coefficient ϕ reduces to a constant when the considered base flows are characterized by a constant temperature gradient, which is not the case for the thermal boundary layer considered here. Moreover, in the present case of the Blasius boundary layer, the potential energy value in Eq. (25) has a peculiar divergent behavior in the free-stream flow region since the derivative of the base-temperature (density) profile with respect to the y coordinate T_b' is zero. Therefore, it is interesting to discuss how this singularity can be overcome and how the different possible approximations of the potential energy term influence the transient energy growth for the case of the Blasius boundary layer. For this purpose, in this work, three approximations of the energy norm have been considered as objective functions of the optimization procedure:

(i) E_1, considering only the contribution of the kinetic energy ($\phi = 0$);

(ii) E_2, in which the derivative of the base-flow temperature field is approximated by a constant value equal to $\Delta \check{T}_b / \check{\delta}_T^\star$, which gives, using Eq. (13) and nondimensionalizing $\phi = \text{Ri}\,\text{Pr}^{-1/3}$;

(iii) E_3, in which $\phi(y)$ is given by Eq. (26) with T_b' equal to the base-flow temperature derivative up to a given wall-normal position $\bar{y}$, whereas, for $y > \bar{y}$, it is fixed to a (small, although nonzero) constant value.

The coefficients ϕ for the three approximations of the energy are plotted in Fig. 2, where, in order to overcome the singularity due to the temperature derivative in the free stream, the minimum value of T_b' for the evaluation of the E_3 norm has been limited to the value of the derivative at $\bar{y} = \delta_T^*$ or $\bar{y} = \delta_{T,99}$, δ_T^* and $\delta_{T,99}$ being the displacement and 99% thicknesses of the thermal boundary layer, respectively. The corresponding norms are denoted as $E_3^{\delta^*}$ and $E_3^{\delta_{99}}$, respectively. Notice that, while in the former case ϕ shows comparable values at the wall and far from it, in the latter case, the value of the coefficient in the free stream is two orders of magnitudes higher than the corresponding value at wall.

Once the energy norm has been defined as in Eq. (25), it should be maximized at a given target time $\bar{t}$ under appropriate constraints. The Lagrange functional can be set up by adding Eqs. (5)–(7) as constraints by means of the Lagrange multipliers, as follows:

$$\mathcal{L}(\mathbf{u}, p, T, \mathbf{u}^\dagger, p^\dagger, T^\dagger, \mathbf{u}(0), \mathbf{u}(\bar{t}), T(0), T(\bar{t}), \lambda)$$

$$= E(\bar{t}) - \int_0^{\bar{t}} \int_V p^\dagger \nabla \cdot \mathbf{u}\, dV\, dt$$

$$-\int_0^{\bar{t}} \int_V \mathbf{u}^\dagger \left(\frac{\partial \mathbf{u}}{\partial t} + (\mathbf{u} \cdot \boldsymbol{\nabla})\mathbf{U}_b + (\mathbf{U}_b \cdot \boldsymbol{\nabla})\mathbf{u} + \boldsymbol{\nabla} p - \frac{1}{\mathrm{Re}} \nabla^2 \mathbf{u} - \mathrm{Ri} T \mathbf{e}_y \right) dV \, dt$$

$$-\int_0^{\bar{t}} \int_V T^\dagger \left(\frac{\partial T}{\partial t} + (\mathbf{u} \cdot \boldsymbol{\nabla})T_b + (\mathbf{U}_b \cdot \boldsymbol{\nabla})T - \frac{1}{\mathrm{Re}\,\mathrm{Pr}} \nabla^2 T \right) dV \, dt - \lambda[E(0) - E_0]. \quad (27)$$

Notice that, for numerical purposes, the initial energy of the perturbation $E(0)$ is fixed to a given value E_0. To maximize the objective function subject to the imposed constraints, the variation of the Lagrange functional with respect to all variables is set to zero. In particular, forcing to zero the variation with respect to the Lagrange multipliers (or adjoint variables $\mathbf{q}^\dagger, \lambda$), provides the imposed constraints. Whereas, nullifying the variation with respect to the direct variables yields, after integration by parts, the following adjoint equations:

$$\frac{\partial \mathcal{L}}{\partial \mathbf{u}} = 0 \;\rightarrow\; -\frac{\partial \mathbf{u}^\dagger}{\partial t} + (\boldsymbol{\nabla}\mathbf{U}_b)^T \mathbf{u}^\dagger - (\mathbf{U}_b \cdot \boldsymbol{\nabla})\mathbf{u}^\dagger - \boldsymbol{\nabla} p^\dagger - \frac{1}{\mathrm{Re}} \nabla^2 \mathbf{u}^\dagger + T^\dagger \boldsymbol{\nabla} T_b = 0, \quad (28)$$

$$\frac{\partial \mathcal{L}}{\partial p} = 0 \;\rightarrow\; \boldsymbol{\nabla} \cdot \mathbf{u}^\dagger = 0, \quad (29)$$

$$\frac{\partial \mathcal{L}}{\partial T} = 0 \;\rightarrow\; -\frac{\partial T^\dagger}{\partial t} - (\mathbf{U}_b \cdot \boldsymbol{\nabla})T^\dagger - \frac{1}{\mathrm{Re}\,\mathrm{Pr}} \nabla^2 T^\dagger - v^\dagger \mathrm{Ri} = 0. \quad (30)$$

Finally, posing to zero the variation with respect to $\mathbf{q}(\bar{t}), \mathbf{q}(0)$ provides the compatibility and gradient conditions, respectively:

$$\frac{\partial \mathcal{L}}{\partial \mathbf{u}(\bar{t})} = 0 \;\rightarrow\; \mathbf{u}(\bar{t}) - \mathbf{u}^\dagger(\bar{t}) = 0; \quad \frac{\partial \mathcal{L}}{\partial T(\bar{t})} = 0 \;\rightarrow\; \phi T(\bar{t}) - T^\dagger(\bar{t}) = 0, \quad (31)$$

$$\frac{\partial \mathcal{L}}{\partial \mathbf{u}(0)} = 0 \;\rightarrow\; \mathbf{u}^\dagger(0) - \lambda \mathbf{u}(0) = 0; \quad \frac{\partial \mathcal{L}}{\partial T(0)} = 0 \;\rightarrow\; T^\dagger(0) - \lambda \phi T(0) = 0. \quad (32)$$

The system of equations (5)–(7), (28)–(30), and (31), (32) constitutes the optimization problem to be solved for obtaining the optimal initial condition providing the maximum gain. The optimization system is solved using a direct-adjoint looping cycle similar to that used in Ref. [29]. The flow variables are first decomposed into a Fourier-Laplace transform in the streamwise and spanwise directions, with α, β being the streamwise and spanwise wave numbers. The direct equations (5)–(7) are integrated in time using a given initial condition; at time $t = \bar{t}$ the compatibility condition (31) provides initial conditions for the adjoint equations (28)–(30), which are integrated backward in time up to $t = 0$. Then, the adjoint variables at time $t = 0$ are used to find the new initial conditions of the direct problem by means of gradient methods or power iteration, making use of Eq. (32), where the λ Lagrange multiplier serves as a normalization parameter for rescaling the perturbation to the imposed initial energy. The direct-adjoint loop is repeated until the difference between the gain obtained in two successive iterations is smaller then the fixed threshold $\epsilon = 10^{-5}$. When convergence for the given target time is achieved, the value of $\bar{t}$ is increased by 2 time units and the direct-adjoint algorithm is restarted by using the previously computed initial optimal solution as initial guess. This allows one to reduce considerably the number of iterations needed for computing the curve of the optimal gain and does not affect the final solution. Temporal discretization of the direct and adjoint equations is carried out using a fully implicit fourth-order accurate backward Euler scheme [30]. The same spatial discretization described in Sec. II B is used, with $N_y = 100$ collocation points for the short-time optimizations, and $N_y = 150$ points for the long-time ones, which require a larger domain (see discussion in Sec. IIIB2). In order to validate the numerical code, we have compared our results with the optimal perturbations found in the literature for the Blasius flow in the absence of thermal stratification [31] and for the stably stratified plane Poiseuille flow [5], finding a very good agreement.
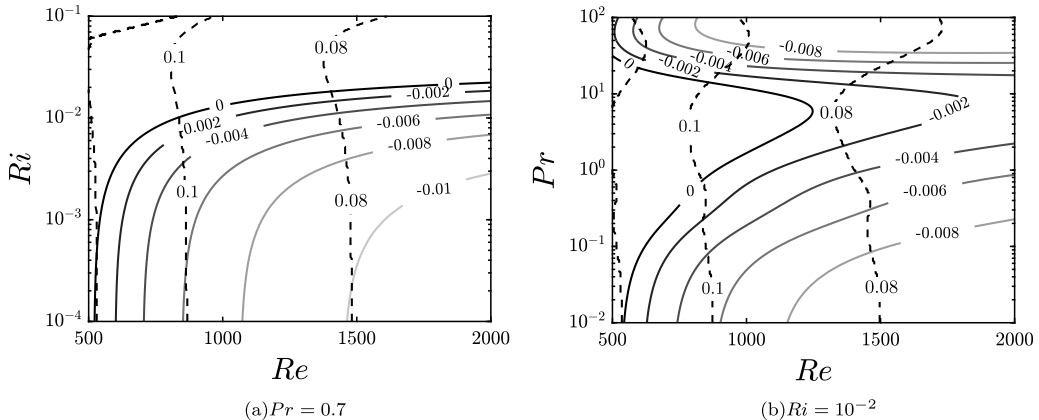
FIG. 3. Richardson and Prandtl number influence on the Blasius flow. Contours of largest growth rate α_i (continuous lines) and corresponding angular frequency ω of largest growth (dashed lines) in the (Re, Ri) plane for Pr = 0.7 (a) and in the (Re, Pr) plane for Ri = 10^{-2} (b). The continuous black line is the neutral stability curve.

III. RESULTS

A. Modal stability analysis

Figure 3 shows the influence of the Richardson and Prandtl numbers on the most unstable spatial mode (continuous lines), which is always found for $\beta = 0$, and the corresponding angular frequency at which the largest growth rate is found (dashed lines). Increasing the Richardson number, the growth rate of the most unstable mode decreases, as already shown in Refs. [2] and [5] in a temporal and spatial framework, respectively, for the plane Poiseuille flow with stable stratification. As expected, also in the case of the boundary layer flow, buoyancy appears to stabilize the flow, strongly influencing the critical value of the Reynolds number. In particular, Re_c is pushed to 829.3 for Ri = 10^{-2}, and considerably increases for Ri $\gtrsim 10^{-2}$, apparently reaching an asymptote for Ri $\approx 2 \times 10^{-2}$. Despite the strong influence of Ri on the value of the critical Reynolds number, the structure of the Tollmien-Schlichting wave appears to be weakly sensitive to buoyancy. Figures 4(a) and 4(b) show the marginally unstable eigenvectors obtained with Pr = 0.7 for two values of the Richardson number Ri = 10^{-4} (with pulsation frequency $\omega = 0.12$ and $Re_c = 519.4$) and Ri = 10^{-2} (with $\omega = 0.1$ and critical Reynolds number equal to 829.3), respectively. Both eigenvectors present a clear Tollmien-Schlichting wave structure, with the velocity components recalling those of the unstratified case, whereas the temperature component shows a peak near the wall and decreases exponentially outside the boundary layer. As observed by Biau and Bottaro [5] for Poiseuille flow, the shape of the eigenvectors as well as the critical streamwise wave number are weakly affected by the Richardson number [for instance, $\alpha_r = 0.303$ in the case shown in Fig. 4(a) and $\alpha_r = 0.277$ in Fig. 4(b)].

Considering the influence of the Prandtl number, Fig. 3(b) shows that this parameter plays an important role in the stability of the Blasius flow, differently from what observed for the plane Poiseuille flow [5]. The critical Reynolds number strongly varies with Pr, at first increasing for $0.01 < Pr < 7$, and then decreasing. To explain such behavior one should notice that, for a fixed Reynolds number, the Prandtl number affects the flow stability in two different ways. The first effect is directly due to its presence in the temperature equation (7): increasing Pr, the diffusion term becomes smaller with respect to the other terms, inducing a reduced stabilization of the temperature component for increasing Pr at fixed Re and Ri, which might explain the behavior found for Pr > 7. At the same time, however, an increase of the Prandtl number with fixed kinematic viscosity translates into a decrease of the thermal diffusivity coefficient κ, indicating that the viscous effects
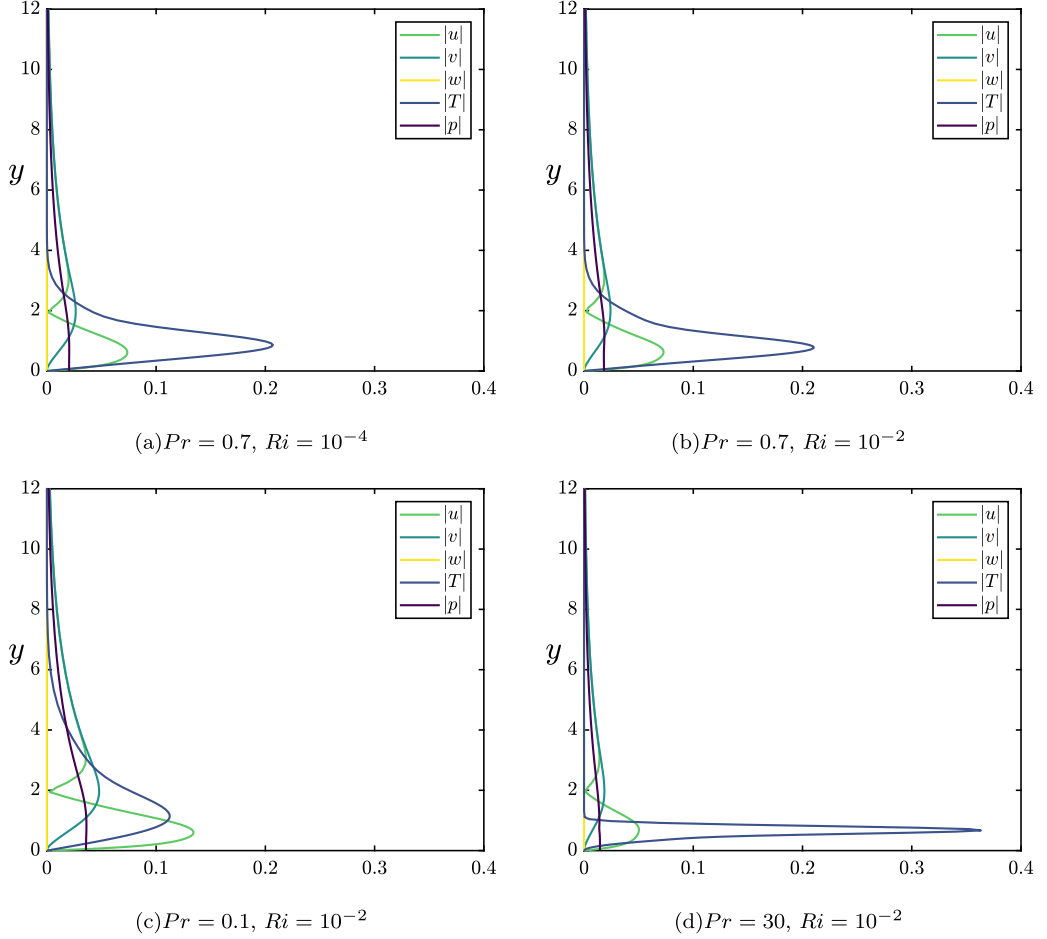
FIG. 4. Absolute value of the five components of the unstable eigenvectors for the stratified Blasius flow at critical conditions (indicated in Table I) for different Richardson and Prandtl numbers.

become predominant with respect to the thermal ones. The unbalance between these two effects leads to an initial stabilization of the flow when increasing Pr from very low values at fixed Re and Ri. Then, a destabilization effect is observed, probably due to the much smaller weight of the thermal diffusion term, when Pr is increased at values larger than 7. This is corroborated by the eigenvector shapes provided in Figs. 4(b)–4(d) for three values of Pr and Ri = 10^{-2}. Comparing Figs. 4(b) and 4(c) one can observe that lowering the Prandtl number in the range 0.01 < Pr < 7 induces a reduction of the temperature component with respect to the velocity ones, due to the predominance of the stabilizing thermal effects. Whereas, increasing Pr to values larger than 7 results in a growth of the temperature component with respect to the velocity ones, consistent with the decreased weight of the diffusion term in the temperature equations which induces a destabilization of the temperature component. In this respect, one should notice that in this case the critical Reynolds number is decreased, but on a much lesser extent compared to the Prandtl number increase, so that the product Re Pr is indeed increased. One can also notice that the Prandtl number influences the wall-normal distribution of the unstable eigenvector profiles, whose peak values move toward the wall when Pr increases, as one can clearly notice in Fig. 5, providing the temperature component profiles of the unstable modes for four different Prandtl numbers. This behavior is most probably linked to the influence of the Prandtl number on the ratio between the thermal boundary layer
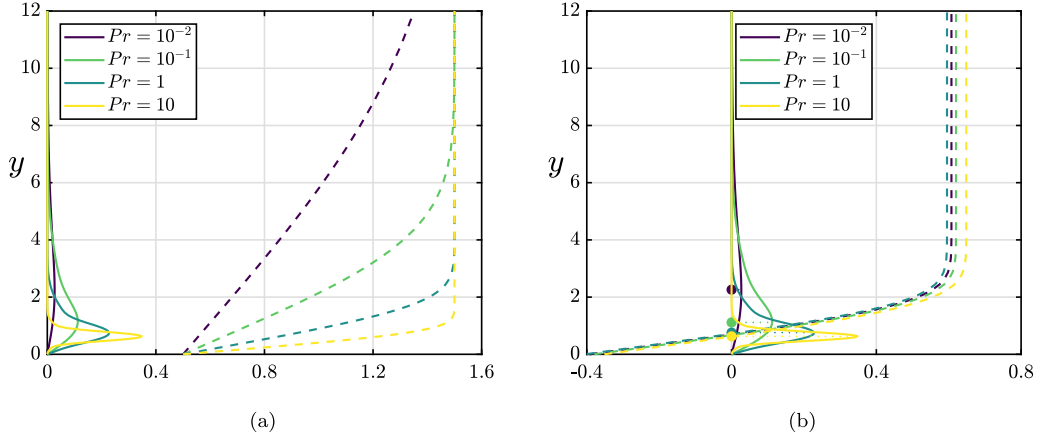
FIG. 5. Temperature component of the unstable eigenvalues (continuous lines in both subfigures) and corresponding (a) temperature and (b) velocity profile of the base flow minus the phase speed of the perturbation (dashed lines) at Ri = 10^{-2} and Re = Re_c [see Fig. 3(b)] for four different values of the Prandtl number (see legend). In (b) the dots indicate the peak location of the temperature component of the eigenvectors, whereas the critical layer position corresponds to the y location for which the dashed curves have zero value.

thickness and the velocity one [see dashed lines in Figs. 5(a) and 5(b), respectively]. Figure 5(b) shows that, for Pr = 10 and 1, the wall-normal position of the temperature peak value is very close to the point at which the phase speed of the perturbation (v_φ) is equal to the base-flow velocity U. This indicates that, for large values of the Prandtl number, for which the temperature and velocity base-flow profiles have comparable thicknesses, the structure of the eigenmode is affected by the critical layer location. Whereas, for decreasing values of Pr, for which the temperature boundary layer is considerably thicker than the velocity one, the temperature perturbation peak departs from the critical layer location, moving upward, where the temperature base-flow profile is still sheared, whereas the velocity one has reached its free-stream value. It thus appears that the thermal boundary layer thickness affects the shape and wall-normal extent of the most unstable eigenmode, although its frequency slightly changes, as provided in Table I. The effect of the Richardson and Prandtl numbers on the neutral curves is reported in Fig. 6, which has been plotted on a Re-F plane, with F defined as $10^6\omega/\mathrm{Re}$, as usually done for the study of the asymptotic spatial stability of boundary layer flows (see, for instance, Ref. [19]) . For Ri = 10^{-4} the neutral curve is almost superposed to that of the unstratified Blasius flow. Increasing this parameter, the unstable area considerably decreases due to the increased role of buoyancy, which has a stabilizing effect in the problem under consideration. Despite the strong decrease of the unstable area, and the considerable increase of the critical Reynolds number, which is reported in Table I, the critical values of α_r and ω do not change much. The same weak influence on the critical wave number is observed when varying the

TABLE I. Critical parameters for different values of Ri and Pr, corresponding to the cases shown in Figs. 4 and 6, compared to the unstratified case (first line).

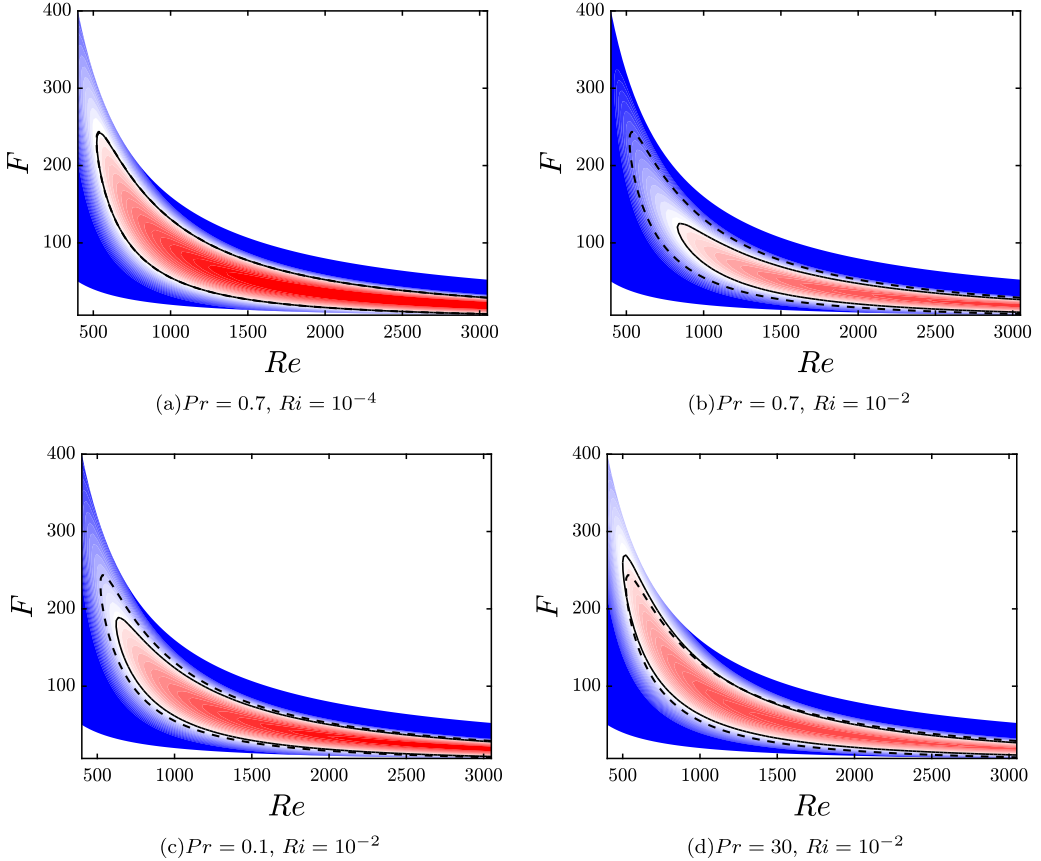| Ri	Pr	Re_c	α_r	ω
		519.4	0.303	0.120
10^{-4}	0.7	519.4	0.303	0.120
10^{-2}	0.7	829.3	0.277	0.101
10^{-2}	0.1	622.5	0.302	0.115
10^{-2}	30	500.0	0.306	0.125

FIG. 6. Isocontours of the spatial growth rate (blue for negative, red for positive values) and neutral curves (solid lines) for different Richardson and Prandtl numbers for the stratified (continuous lines) and unstratified (dashed lines) Blasius flow. The critical conditions are indicated in Table I.

Prandtl number, as reported in Table I. Whereas, the unstable area of the neutral curve decreases when increasing Pr from 0.1 to 0.7, and then increases again for Pr = 30.

B. Nonmodal stability analysis

In this section, the results of the transient growth analysis are provided, focusing at first on the short-time behavior $[t \approx O(10)]$, and then, in a few selected cases, also on the long-time dynamics $[t \approx O(10^3)]$. As will be discussed in more detail in Sec. IIIB2, the short-time dynamics is practically independent of the definition of the energy norm introduced before, the optimal gain being affected by less then 0.1% by the choice of the norm approximation. Thus, in Sec. IIIB1 the influence of the energy norm on the results will not be considered; whereas, a thorough discussion of the effect of the norm on the long-time energy growth will be provided in Sec. IIIB2.

1. Short-time energy amplification

The short-time optimizations are performed for several values of the nondimensional parameters Ri, Re, Pr in order to unravel the effect of the different physical mechanisms that may affect the energy growth in a Blasius flow subject to stable stratification. All these computations have been carried out for the norm E_2, although it has been verified in many of the considered cases that using different norm approximations provides virtually the same results. At first, the influence of the
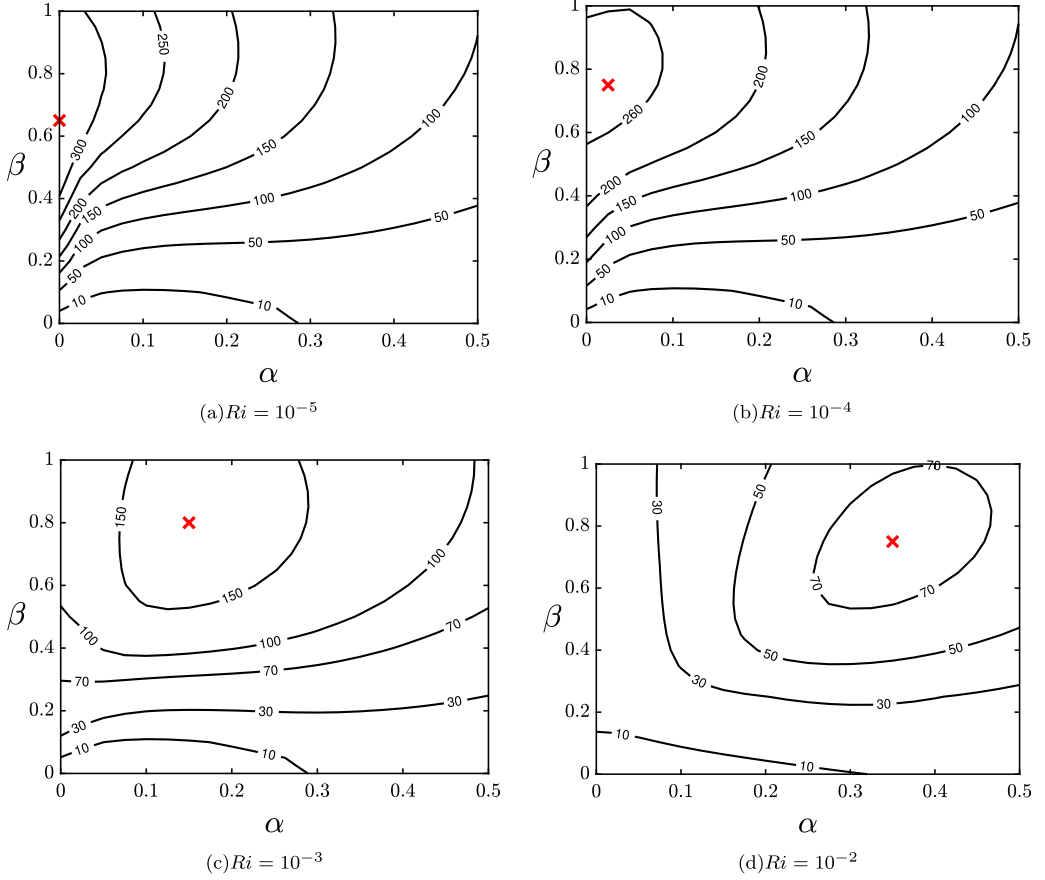
FIG. 7. Optimal gain contours G_{opt} as a function of the streamwise wave number α and the spanwise wave numbers β, at fixed Reynolds number Re = 500 and Prandtl number Pr = 0.7 for different Richardson numbers (Ri = 10^{-5}, 10^{-4}, 10^{-3}, 10^{-2}). The red cross symbols indicate the conditions of optimal growth.

buoyancy effect on transient growth mechanisms is investigated by varying the Richardson number at fixed Re and Pr.

For each considered value of the Richardson number, we evaluate the optimal growth G_{opt} and optimal time t_{opt}, defined as the smallest time at which the gain curve peaks, for several streamwise and spanwise wave numbers, in order to identify the conditions of maximum energy growth. Figure 7 shows the contour levels of the optimal gain G_{opt} for $0 < \alpha < 0.5$ and $0 < \beta < 1$ at fixed Reynolds number Re = 500 and Prandtl number Pr = 0.7 for different Richardson numbers (Ri = 10^{-5}, 10^{-4}, 10^{-3}, 10^{-2}). In particular, the largest considered value of the Richardson number has been chosen so as to be comparable with that of nocturnal atmospheric boundary layer flows in weakly stable conditions, which present Ri < 0.1 near the surface. Whereas, the other values of Ri have been chosen so as to provide a continuous transition between this reference case and the unstratified boundary layer flow. For the lowest value of Ri, the optimal gain (indicated by the red cross symbol corresponding to $G_{\text{opt}} = 361.88$) is found for $\alpha = 0$ and $\beta = 0.65$, matching the optimal streamwise and spanwise wave numbers found for the unstratified Blasius flow [31]. In this case, the initial perturbation providing the maximum energy growth of the system is a pair of counter-rotating streamwise-independent vortices, giving rise at optimal time to elongated low- and high-momentum regions alternating in the spanwise direction, namely, a pair of *streaks*, due to
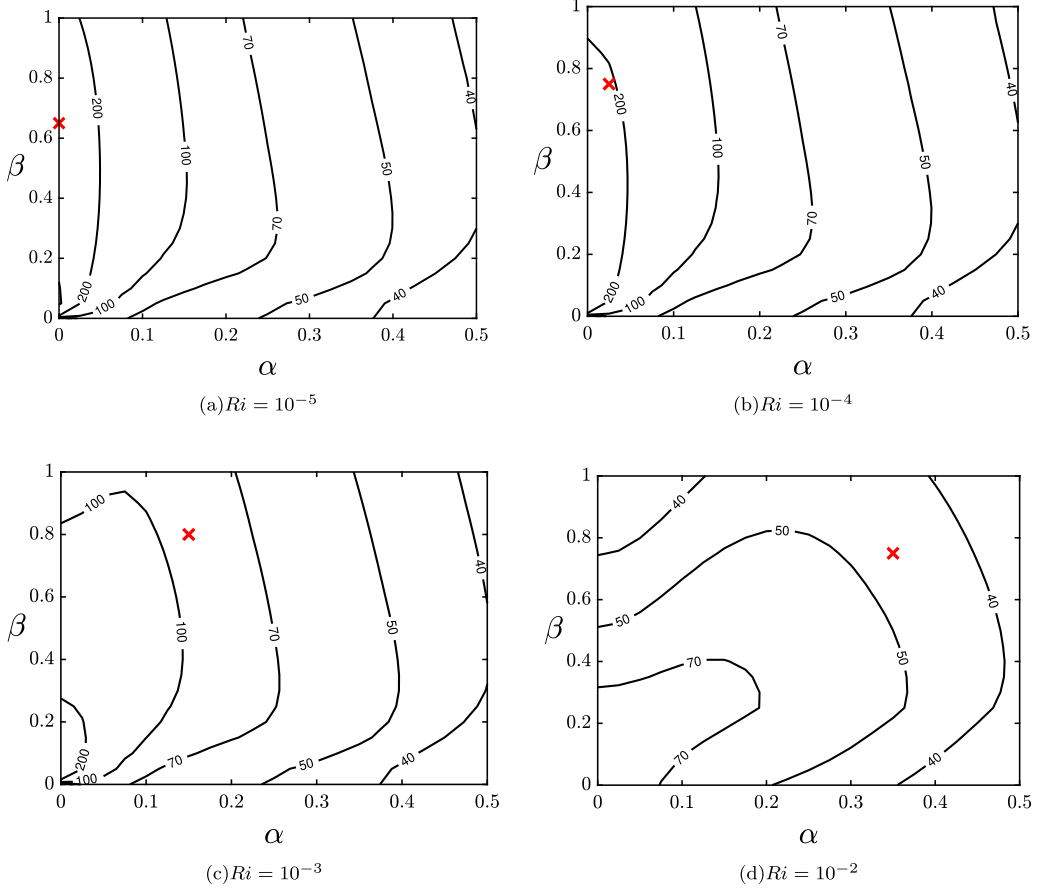
FIG. 8. Optimal time contours t_{opt} as a function of the streamwise α and the spanwise β wave numbers at fixed Reynolds number Re $= 500$ and Prandtl number Pr $= 0.7$ for different Richardson numbers (Ri $= 10^{-5}$, 10^{-4}, 10^{-3}, 10^{-2}). The red cross symbol indicates the conditions of optimal growth.

the so-called lift-up mechanism [32]. Increasing the Richardson number, due to the non-negligible effect of buoyancy, the optimal streamwise wave number considerably departs from zero, reaching $\alpha = 0.35$ for Ri $= 10^{-2}$. Whereas, the spanwise wave number changes more slightly with the Richardson number, achieving the maximum value $\beta = 0.8$ for Ri $= 10^{-3}$. Thus, stable thermal stratification introduces a streamwise modulation of the optimal perturbation, with the wave number increasing with Ri, but also induces a considerable drop of the optimal gain, which decreases to $G_{\mathrm{opt}} = 75.5$ for the largest considered value of Ri. A strong effect of the Richardson number is found also on the optimal time, t_{opt}, which is provided in Fig. 8 as a function of α and β for four values of Ri. In particular, for small values of Ri, the optimal time is barely dependent on the value of β in the range $0.2 < \beta < 1$, while it decreases for $\beta < 0.2$. In all cases, t_{opt} strongly increases when α approaches zero. Whereas, for higher values of the Richardson number, t_{opt} depends on the spanwise wave number too, showing a nontrivial behavior. This indicates that when buoyancy effects are relevant, the amplification mechanism at work may no longer be the lift-up effect only since thermal stratification may render other energy growth mechanisms, not relying on the generation of streamwise-independent flow structures, more relevant.

Figures 9(a) and 9(b) show the influence of the Richardson number on the optimal gain and optimal time for different values of the Reynolds number. The curves are obtained for Pr $= 0.7$.
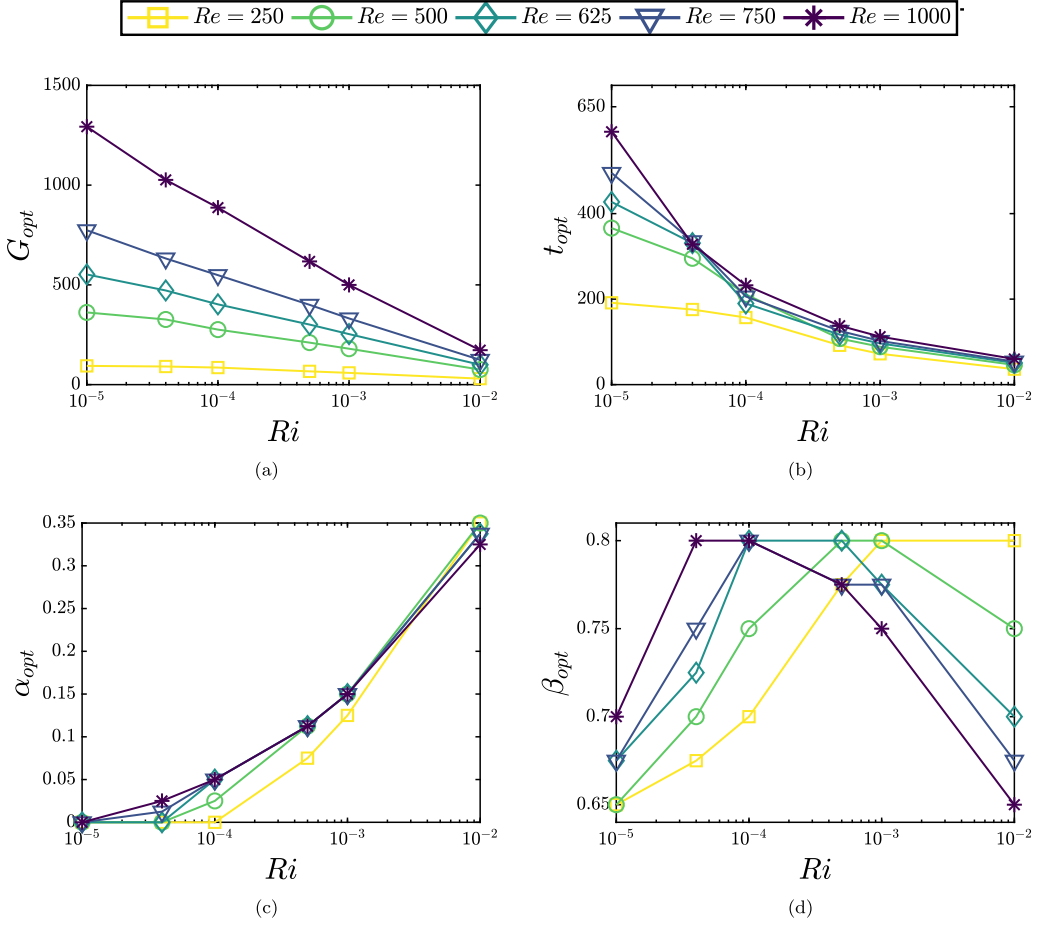
FIG. 9. Optimal gain G_{opt} (a), optimal time t_{opt} (b), optimal streamwise wave number α_{opt} (c), and optimal spanwise wave number β_{opt} (d) trends with the Richardson number Ri for different values of Reynolds number Re at fixed Prandtl number Pr = 0.7.

Both the optimal energy gain and the optimal time decrease when the buoyancy effect increases. Concerning the optimal energy gain, this effect is stronger for larger values of the Reynolds number since the energy gain appears to decrease linearly with the logarithm of Ri, but with a slope that increases with Re, following, for Ri > 0, a logarithmic law,

$$G_{\text{opt}} \approx -A(\text{Re}) \log_{10} \text{Ri} - B(\text{Re}), \tag{33}$$

where A and B both increase with Re. A similar, although not identical behavior has been found in [33], in which for stratified mixing layers the maximum perturbation gain has been found to increase with Re and decrease with the Richardson number. Similarly, the optimal time decreases with the logarithm of Ri. A quasilinear trend with steeper slope as Re increases is observed at low values of Ri. On the contrary, for Ri > 5×10^{-4}, the effect of the Richardson number on the optimal time tends to be independent of Re, and the t_{opt} curves obtained for different values of Re collapse onto each other. Figure 9(c) shows the variation of the streamwise wave number α versus Ri for different values of Re. In all cases, α is found to increase with the Richardson number, although its departure from zero occurs at larger values of Ri when the Reynolds number is low. Whereas, for large values of Re the curves tend to collapse onto each other. Finally, the influence of Ri on the
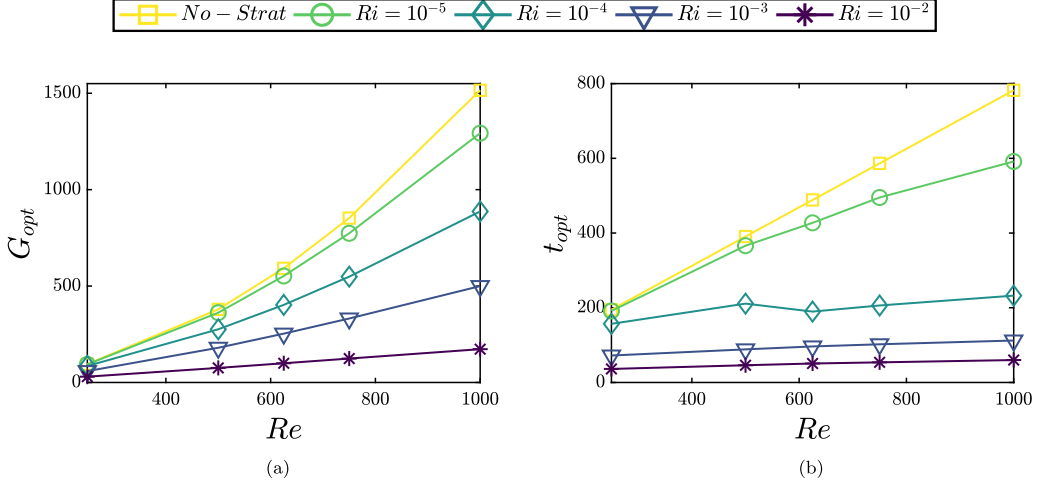
FIG. 10. Optimal gain G_{opt} (a) and optimal time t_{opt} (b) trends with the Reynolds number Re for different values of Richardson number Ri at fixed Prandtl number Pr = 0.7.

spanwise optimal wave number is shown in Fig. 9(d). For low values of the Reynolds number, β_{opt} gradually increases with Ri, peaking for Ri $\geqslant 10^{-3}$. Whereas, for increasing values of Re, the value of the spanwise wave number is found to peak at lower values of Ri. Thus, the optimal perturbation shape appears to be nontrivially influenced by the Richardson and Reynolds numbers.

Figure 10 shows the Reynolds number influence on the optimal gain and optimal time for different values of the Richardson number. It is known that, in unstratified shear flows such as the Blasius boundary layer, the spanwise wave number is independent of Re [34], the optimal gain presents a quadratic dependence on the Reynolds number, whereas the optimal time shows a linear dependence with Re [35], associated with the lift-up mechanism [36]. Stable stratification appears to break these dependencies on Re since the optimal gain tends to a linear behavior with respect to the Reynolds number and the optimal time tends to be independent of Re when increasing the Richardson numbers. This, together with the increase of the streamwise wave number with Ri, suggests that the optimal amplification mechanism of a boundary layer in the presence of a stable stratification is no longer the lift-up. Finally, the Prandtl number influence on the optimal energy gain for the stratified Blasius flows is shown in Fig. 11(a). One can observe that, varying this nondimensional parameter in the range $0.7 < \text{Pr} < 7$, the optimal gain is barely affected by the thermal effect. A similar conclusion can be drawn concerning the influence of Pr on the optimal time provided in Fig. 11(b), although for intermediate values of Ri the optimal time is found to slightly increase with Pr.

In order to investigate the nature of the optimal amplification mechanisms in the presence of a sufficiently strong stable stratification, we analyze in detail the behavior of the flow at Re = 500, Ri = 10^{-3}, and Pr = 0.7. In this particular case, the optimal perturbation has optimal streamwise and spanwise wave numbers $\alpha = 0.15$ and $\beta = 0.8$, respectively. Figure 12(a) reports the optimal gain envelope (continuous line), peaking at $t_{opt} = 88.62$, for which the optimal gain $G_{opt} = 180.03$ is obtained, together with the time evolution of the gain G computed by time marching the optimal perturbations obtained for three different target times (dashed lines). Clearly, smaller values of the gain are obtained for target times smaller or larger then t_{opt}, although the overall shape of the energy gain curve and the related optimal perturbations are very similar. A three-dimensional view of the streamwise velocity perturbation at optimal time t_{opt} is provided in Fig. 12(b), showing the presence of oblique elongated structures, remnants of the lift-up mechanism, but having a finite inclination with respect to the streamwise direction. Figure 13(a) reports the wall-normal
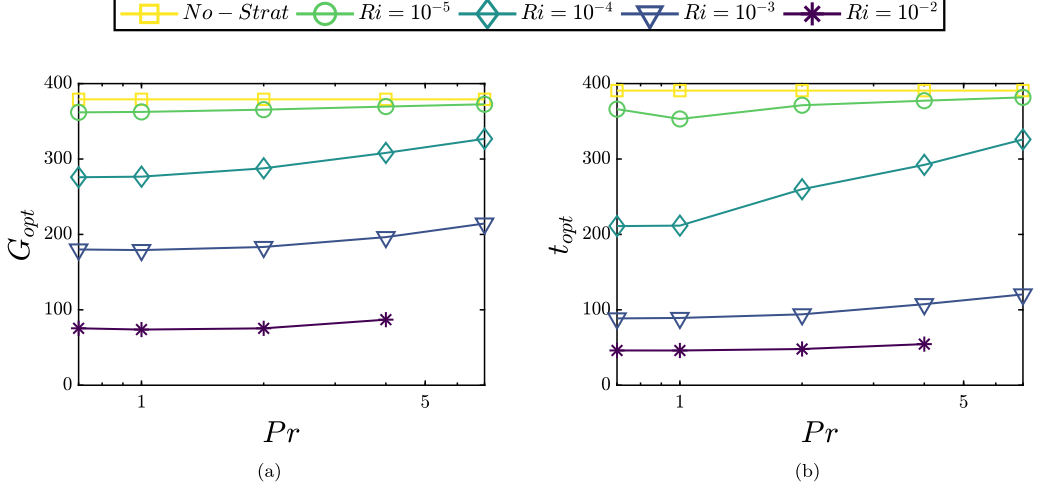
FIG. 11. Optimal gain G_{opt} (a) and optimal time t_{opt} (b) trends with the Prandtl number Pr for different values of Richardson number Ri at fixed Reynolds number Re $= 500$.

profiles of the initial optimal perturbation. As expected in the presence of the lift-up mechanism, the components of largest amplitude are the spanwise and wall-normal ones, that are responsible for the counter-rotating vortex formation. However, the streamwise velocity component is not negligible, having almost the same amplitude of the wall-normal one. The wall-normal profiles of the optimal perturbation at optimal time are provided in Fig. 13(b) showing that the temperature and the streamwise velocity are the main components of the optimal perturbation, indicating the presence of temperature-inclined streaks associated with the streamwise velocity ones. As typically occurs in the case of the lift-up mechanism, the cross-flow velocity components $v - w$ are small, at least compared with the streamwise and temperature ones. However, these components present
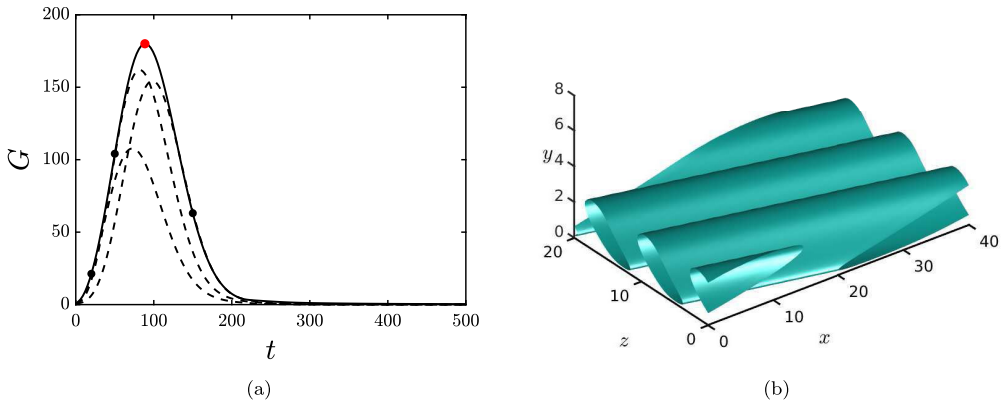

FIG. 12. (a) Envelope of the optimal energy gain versus time (continuous line) and time evolution of the gain for three optimal perturbations obtained for target times $\bar{t} = 20, 50, 150$ (dashed lines from left to right, the black dots indicate the optimal gain obtained for each of the given target times). (b) Three-dimensional view of the streamwise velocity perturbation at the optimal time $\bar{t} = t_{opt} = 88.62$ [red dot in (a)]. The optimizations have been performed at fixed Richardson number Ri $= 10^{-3}$, Reynolds number Re $= 500$, Prandtl number Pr $= 0.7$, streamwise wave number $\alpha = 0.15$, and spanwise wave number $\beta = 0.8$.
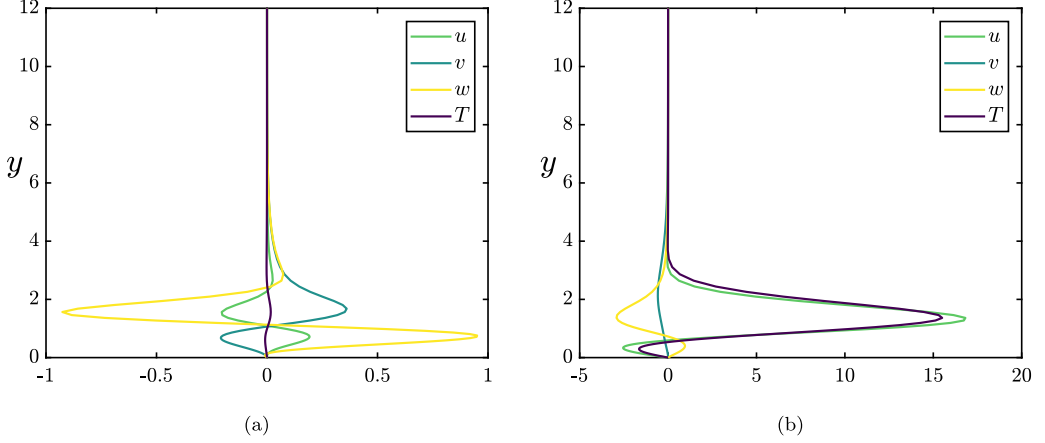
FIG. 13. Wall-normal profiles of the optimal disturbance at (a) $t = 0$ and (b) at the optimal time $t = t_{\text{opt}}$, for Richardson number $\text{Ri} = 10^{-3}$, Reynolds number $\text{Re} = 500$, Prandtl number $\text{Pr} = 0.7$, streamwise wave number $\alpha = 0.15$, and spanwise wave number $\beta = 0.8$.

negative values in the near-wall region, indicating that a different amplification mechanism may be active too.

The two-dimensional contours of u in the x-y plane are provided in Fig. 14 at four different times during the flow evolution, showing that the streamwise velocity perturbation, initially inclined against the shear, is tilted in the direction of the shear as time evolves. This peculiar evolution indicates the presence of the Orr mechanism [37], which provides an increase of the spanwise vorticity (and thus of the u-v perturbation components) due to the conservation of circulation in an xy plane. To investigate the reasons of the presence of the Orr mechanism, we run two additional optimizations by constraining the perturbation on an xy plane (where only the Orr mechanism is active) and then on a yz plane (where only the lift-up is). Thus, we perform optimizations for $\alpha = 0$ and then for $\beta = 0$, at different Richardson numbers, for $\text{Re} = 500$ and $\text{Pr} = 0.7$. Increasing the Richardson number, the optimal time associated with the lift-up mechanism strongly decreases reaching the optimal time for the Orr mechanism at $\text{Ri} = 10^{-2}$, as shown in Fig. 15. This explains the simultaneous presence of the Orr and lift-up mechanisms when the buoyancy term is sufficiently high.

To investigate the reason why the Orr mechanism becomes "competitive" with the lift-up as the Richardson number increases, we measure the time evolution of the production terms of the Reynolds-Orr equation extended to the stratified flow case:

$$\frac{dE_c}{dt} = \underbrace{-\int_V \mathbf{u} \cdot (\mathbf{u} \cdot \nabla)\mathbf{U}_b \, dV}_{\text{Shear production } P_s} \underbrace{-\frac{1}{\text{Re}} \int_V \nabla\mathbf{u} : \nabla\mathbf{u} \, dV}_{\text{Viscous dissipation } D_v} + \underbrace{\text{Ri} \int_V \mathbf{u} \cdot \mathbf{e}_y T \, dV}_{\text{Buoyancy flux production } P_b} , \qquad (34)$$

$$\frac{dE_p}{dt} = \underbrace{-\int_V T(\mathbf{u} \cdot \nabla)T_b \, dV}_{\text{Temperature production } P_T} \underbrace{-\frac{1}{\text{Re Pr}} \int_V \nabla T \cdot \nabla T \, dV}_{\text{Thermal dissipation } D_T}. \qquad (35)$$

Figure 16 shows the time evolution of the shear production (left) and buoyancy flux production (right) terms induced by the optimal perturbations at different Richardson number for $\text{Re} = 500$ and $\text{Pr} = 0.7$. Increasing the Richardson number, the shear production, which is usually linked to the lift-up mechanism, peaks earlier in time, suggesting that stable stratification tends to counterbalance the production due to the lift-up mechanism. In fact, inspecting Eq. (35), we can observe that, for inducing an increase of the potential energy due to the temperature production term (namely,
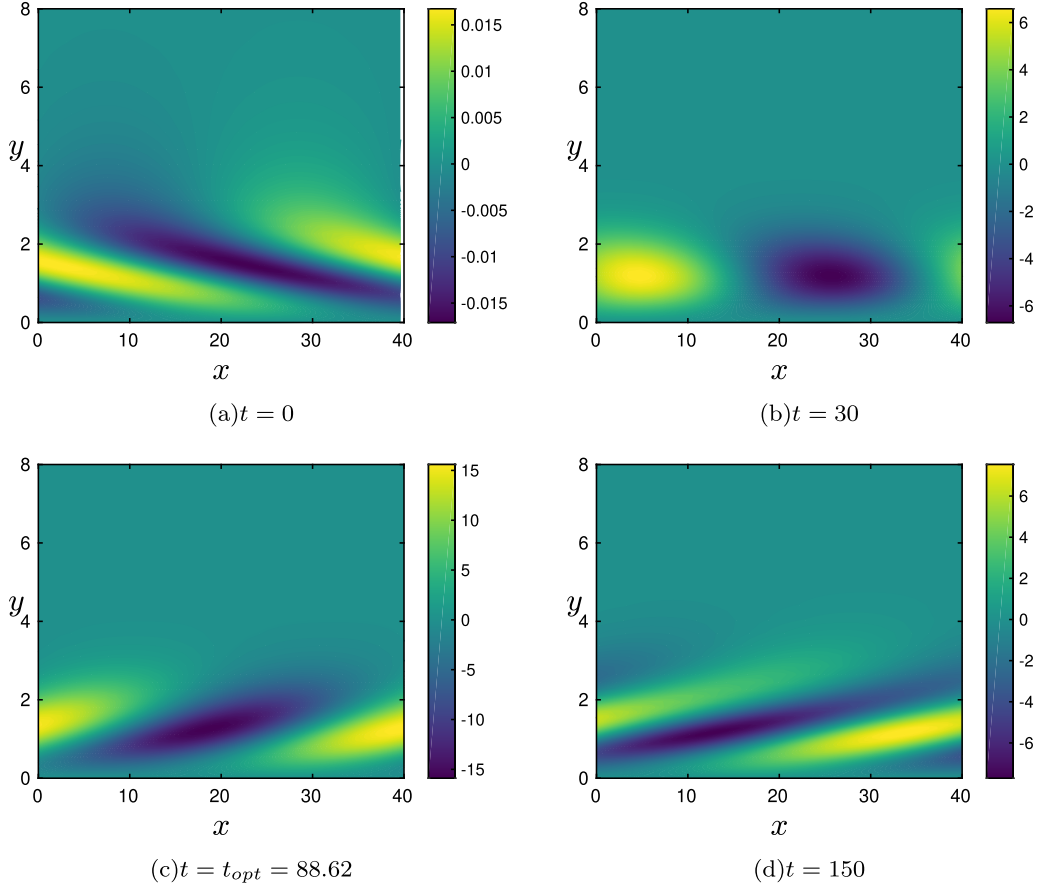
FIG. 14. Streamwise velocity evolution in xy plane of the optimal perturbation at four different times: $t = 0$, $t = 30$, $t = t_{\mathrm{opt}} = 88.62$, and $t = 150$. At fixed Richardson number $\mathrm{Ri} = 10^{-3}$, Reynolds number $\mathrm{Re} = 500$, Prandtl number $\mathrm{Pr} = 0.7$, streamwise wave number $\alpha = 0.15$, and spanwise wave number $\beta = 0.8$.
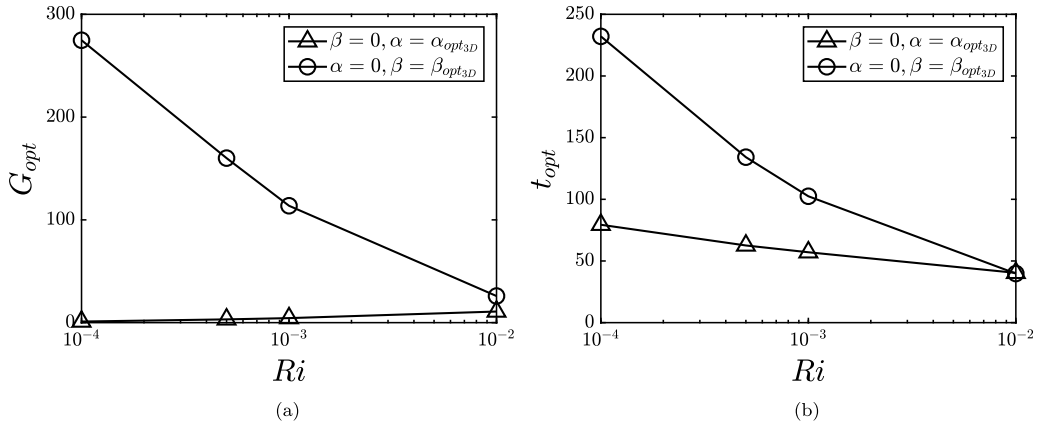

FIG. 15. Richardson number influence on the optimal gain (a) and optimal time (b) for two-dimensional perturbations with (triangles) $\beta = 0$, $\alpha = \alpha_{\mathrm{opt\,3D}}$, and (circles) $\alpha = 0$, $\beta = \beta_{\mathrm{opt\,3D}}$ for $\mathrm{Re} = 500$, $\mathrm{Pr} = 0.7$.
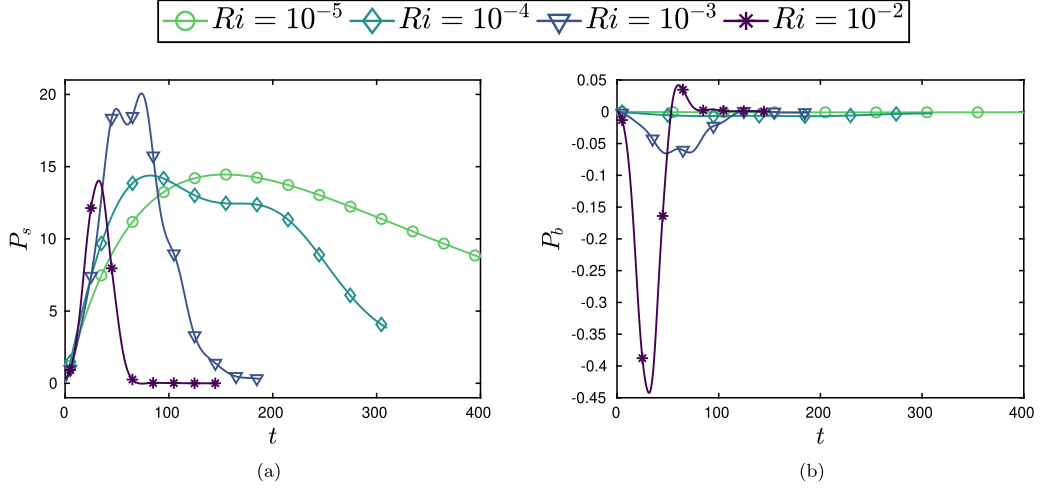
FIG. 16. Shear production (a) and vertical buoyancy flux production (b) for different Richardson numbers: $Ri = 10^{-5}$, $Ri = 10^{-4}$, $Ri = 10^{-3}$, $Ri = 10^{-2}$ at fixed Reynolds number $Re = 500$ and Prandtl number $Pr = 0.7$.

for inducing the equivalent of the lift-up effect on the temperature component), the wall-normal component of the velocity perturbation should be negative in the regions where the wall-normal gradient of temperature is positive (namely, within the boundary layer). As a consequence, the buoyancy flux production term in Eq. (34) becomes negative, with increasing modulus since T is growing due to the increase of the potential energy. Therefore, as time increases, the buoyancy flux production begins to counterbalance the shear production term in Eq. (34), hindering the increase of the kinetic energy due to the classical lift-up mechanism. Thus, to maximize the energy growth, the optimal perturbation tends to induce a rapid increase of the shear (and temperature) production terms, on a timescale sufficiently short not to be counterbalanced by the buoyancy flux production. Therefore, since on a short timescale the energy growth due to the Orr mechanism is of the same order of that due to the lift-up, the two mechanisms are active at the same time for sufficiently high Richardson numbers. The simultaneous presence of these two energy growth mechanisms leads to an optimal perturbation able to exploit both effects via inclined counter-rotating vortices, tilted against the base-flow direction. It is worth remarking that large amplification of three-dimensional oblique wave perturbations for very short times is achieved in many plane shear flows [38] since the wall-normal perturbation velocity produced by the Orr mechanism, active at very short times, induces the growth of the streamwise component through the lift-up mechanism. Although this interplay of Orr and lift-up mechanisms is found to be the overall optimal one for an unbounded infinite-shear flow [38] and a piecewise shear flow with free surface at low Froude number [39], in most of the shear flows it only produces a suboptimal energy growth. For instance, in the mixing layer [13], the same synergistic mechanism, occurring at short timescales, is eventually surpassed by the growth of two-dimensional Kelvin-Helmholtz–type perturbations. In wall-bounded shear flows such as the Couette, the plane Poiseuille. and the boundary layer flow, of interest here, it is overcome by the (much higher) energy growth of two-dimensional streaks occurring at larger timescales [34]. In the present case, stable stratification damps the long-time lift-up mechanism and produces a reduction of its "optimal" timescale in order to avoid a too strong growth of the (negative) buoyancy production term. Increasing the Richardson number, the buoyancy effects become preponderant with respect to the shear production ones and, consequently, the Orr mechanism becomes preponderant on the lift-up one, causing a decrease of the optimal gain and time, an increase of the streamwise wave number, and a different dependence of these parameters on the Reynolds number, as reported in Fig. 10.
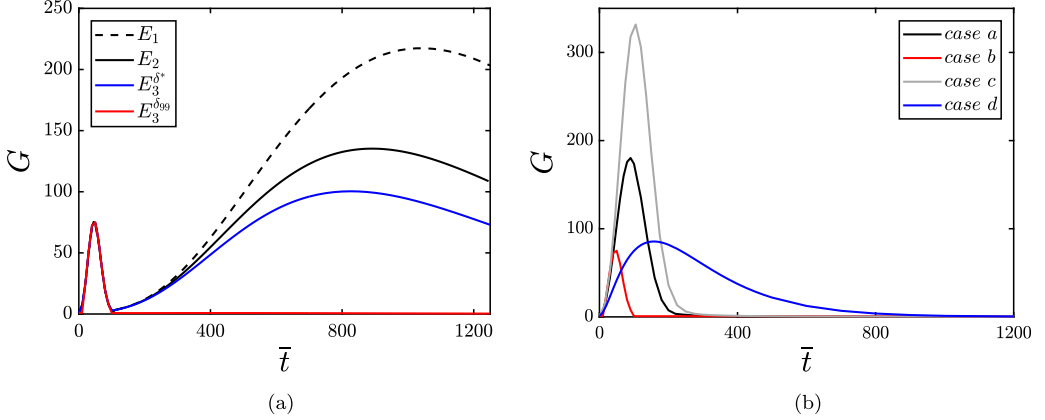
FIG. 17. Envelope of the optimal energy gain G versus the target time $\bar{t}$ for (a) $Ri = 10^{-2}$, $Re = 500$, $Pr = 0.7$, $\alpha = 0.35$, $\beta = 0.75$, and domain size $L_y = 100$ for all the norm approximations considered (see legend within the figure) and for (b) (case a, black line) $Ri = 10^{-3}$, $Re = 500$, $Pr = 0.7$, $\alpha = 0.15$, $\beta = 0.8$; (case b, red line) $Ri = 10^{-3}$, $Re = 500$, $Pr = 0.7$, $\alpha = 0.35$, $\beta = 0.75$; (case c, gray line), $Ri = 10^{-3}$, $Re = 750$, $Pr = 0.7$, $\alpha = 0.15$, $\beta = 0.775$; (case d, blue line) $Re = 250$, $Ri = 10^{-4}$, $Pr = 0.7$, $\alpha = 0$, $\beta = 0.7$.

2. Long-time energy amplification

Inspection of Eqs. (34) and (35) indicates that, apart from the short-time energy growth mechanism that we have discussed in the previous subsection, it is possible to induce an increase of the kinetic energy directly via the buoyancy production term. This can be accomplished by a positive wall-normal velocity perturbation which, coupled with the temperature disturbance, leads to an increase of the (positive) value of the buoyancy production term. However, on a short timescale, this effect will be counterbalanced by the lift-up and Orr mechanisms, for which a positive wall-normal disturbance in the regions where the temperature gradient is positive translates into a decrease of the potential energy. Nevertheless, such transient energy growth might be possible at long timescales when the lift-up and Orr effects fade away. Thus, we have investigated such a possibility by performing optimizations for much larger target times using the different approximations of the energy norm introduced in Sec. II. The black continuous line in Fig. 17 provides the envelope of the optimal energy gain, approximated as $E_2(\bar{t})/E_2(0)$, at different values of the target time $\bar{t}$ ranging from $\bar{t} = 10$ to 1300, for $Ri = 10^{-2}$, $Re = 500$, and $Pr = 0.7$. For this value of the Richardson number, a second energy peak arises at a long time (the long-time optimal time for this case being $t_{opt}^l = 889.16$), whose value of G is larger than that of the first peak. We have to remark that, having observed an increase of both the optimal gain and time, G_{opt}^l and t_{opt}^l, with the wall-normal domain size up to $L_y \approx 60$, we have used $L_y = 100$ for all the computations of this section to avoid any influence of the domain size on the results. Figure 18 shows the wall-normal profiles of the optimal perturbation for $Ri = 10^{-2}$, $Re = 500$, and $Pr = 0.7$, at initial and optimal times. At $t = 0$, the streamwise and spanwise components of the velocity are close to zero, whereas, as expected, temperature and wall-normal velocity have the same sign and peak at the same wall-normal position, right at the center of the region where the temperature base profile has null gradient. In fact, as previously discussed, a positive wall-normal velocity perturbation in the region of positive temperature gradient (i.e., within the boundary layer), will induce a decrease of the potential energy, which will reduce the growth of the objective function. At optimal time, v and T have still the same sign, although both are negative, and u and w have increased amplitude, presenting a negative (positive) value in the upper (lower) part of the domain. A vector plot in the x-y plane, provided in Fig. 19, shows the presence of two counter-rotating vortices, constituted mostly by negative wall-normal velocities pushing negative temperature perturbations toward the boundary
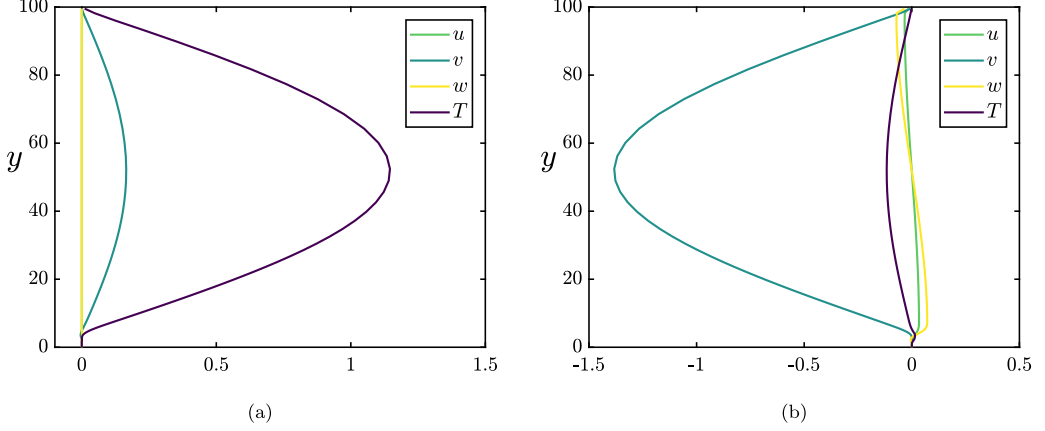
FIG. 18. Shape of the optimal disturbance at (a) $t = 0$ and (b) at the optimal time associated with the second peak $t = t_{opt}^l = 889.16$. The solution is obtained for $Ri = 10^{-2}$, $Re = 500$, $Pr = 0.7$, $\alpha = 0.35$, $\beta = 0.75$, and $L_y = 100$.

layer region, and positive wall-normal disturbances lifting up positive temperature fluctuations. The fact that the wall-normal velocity and temperature disturbances have the same sign confirms that the energy growth is due to the increase of the buoyancy production term, as shown in Fig. 20 providing the energy budget for this long-time optimal solution, compared to the short-time one computed with the same parameters (first peak at $t_{opt} = 46.1$ with $G_{opt} = 75.5$, second peak at $t_{opt}^l = 889.16$ with $G_{opt}^l = 133.24$).

The exploration of the wave-number space shows that the maximum energy growth due to such mechanism is observed for $\beta = 0$ and for a streamwise wave number $\alpha = 0.07$ leading to the emergence of circular cells in the x-y plane. In this particular case, at $Re = 500$, $Ri = 10^{-2}$, and $Pr = 0.7$, an energy gain reaching order 10^6 is found at $t_{opt}^l \approx 10^5$. Moreover, the long-time growth weakens considerably for decreasing values of the Richardson number, completely disappearing for $Ri = 10^{-4}$.

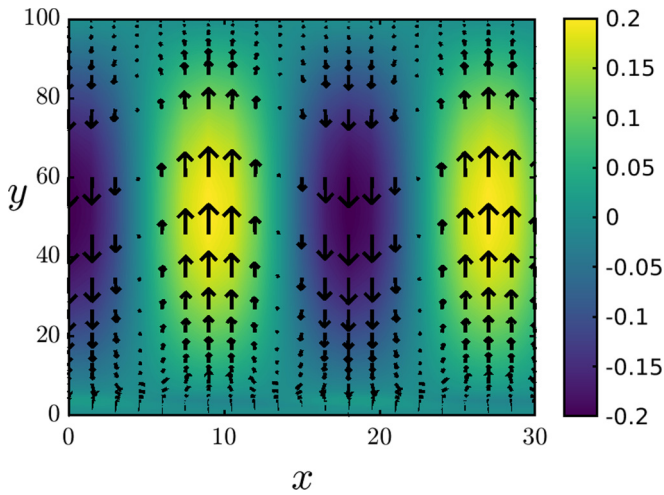
FIG. 19. Contours of temperature, with the black arrows denoting the velocity field in the $x - y$ plane of the optimal disturbance at $t_{opt}^l = 889.16$ on a $x - y$ plane for $Ri = 10^{-2}$, $Re = 500$, $Pr = 0.7$, $\alpha = 0.35$, $\beta = 0.75$, and $L_y = 100$.
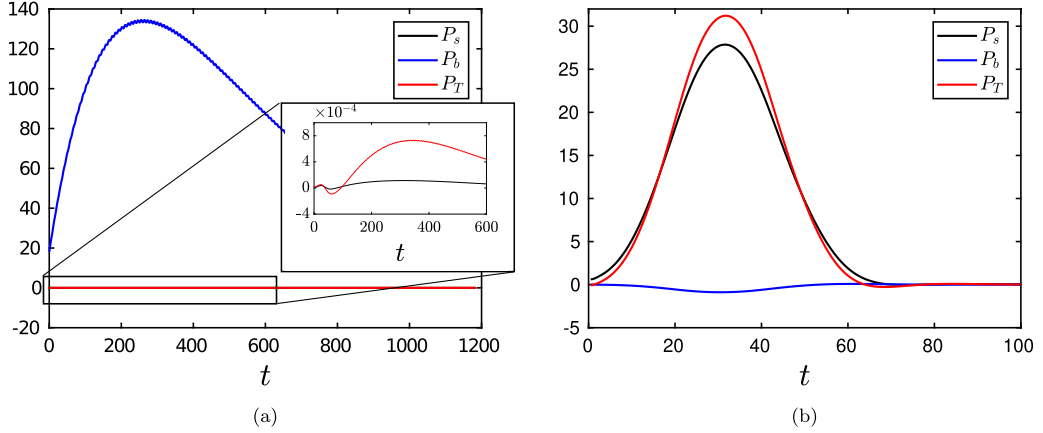
FIG. 20. Energy budget comparison for the optimal perturbations associated to the long-time peak (a) and short-time one (b) at $Ri = 10^{-2}$, $Re = 500$, $Pr = 0.7$, $\alpha = 0.35$, $\beta = 0.75$: shear production P_s, buoyancy flux production P_b, and temperature production P_T evolution in time.

Thus, it appears that a different energy growth mechanism is active at long times, linked to the coupling of temperature and wall-normal velocity fluctuations mediated by the Richardson number, and characterized by a very different timescale with respect to the energy growth mechanisms due to the transport of shear by the perturbations. However, this mechanism appears to be strongly dependent on the choice of the energy norm approximation, as suggested by the colored curves of Fig. 17(a). When the kinetic energy E_1 is optimized, neglecting the contribution of the potential energy to the overall energy growth, the second peak is found to increase together with the optimal time. Whereas, taking into account the potential energy translates into a decrease of the optimal energy gain and time, which tends to zero when the variation of stratification strength height is approximated in an increasingly accurate way. Notice that when the free-stream temperature gradient in the energy norm is approximated by its value at $y = \delta_T^*$ (i.e., when $E_3^{\delta^*}$ is optimized) similar results to those recovered with a linear approximation of the temperature variation with height (i.e., for an E_2 optimization) are found. Instead, when approximating the free-stream temperature gradient with its value at $y = \delta_{T\,99}$, the second peak disappears, indicating that this long-term amplification, although still possible, is not an optimal mechanism. The right panel of Fig. 17 shows that this disappearance of the second peak is not due to the chosen values of Re, Ri, Pr, neither on the choice of α and β, but is a general feature observed when optimizing $E_3^{\delta_{99}}$. This difference in the results obtained using different norm approximations is due to the different values of $\phi(y)$ used in Eq. (25), which is two orders of magnitude higher at the free stream for the $E_3^{\delta_{99}}$ approximation with respect to the other cases. In fact, an increase of the parameter ϕ results into a much larger weight of the initial temperature disturbances with respect to the velocity ones. This effect can be seen in Fig. 21 showing the time evolution of the temperature and wall-normal velocity components of the long-time optimal perturbation for the three norms E_1, E_2, $E_3^{\delta^*}$, all scaled for the same given initial energy E_0. The three curves show the same oscillating behavior linked to the streamwise advection of the rolls shown in Fig. 19. Moreover, one can see that the initial amplitude of the temperature perturbation decreases from E_1 to E_3, due to its increased weight with respect to a velocity disturbance. This induces a reduction of the buoyancy flux production term in the energy equations (34), which depends on the coupling between T and v, weakening the long-time energy gain. When the $E_3^{\delta_{99}}$ norm is used, the weight of a temperature perturbation placed at the free stream becomes huge with respect to that of the velocity ones since ϕ increases of two orders of magnitude from the wall to the free stream. As a consequence, the optimization algorithm places most of the initial energy on velocity disturbances, hindering the coupling between temperature and wall-normal velocity disturbances at the free stream, thus canceling the long-time energy peak. One should also
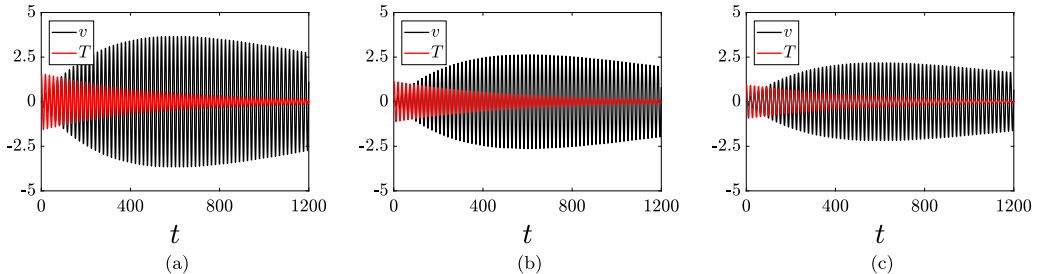
FIG. 21. Time evolution of the wall-normal velocity and temperature components of the long-time optimal disturbance extracted at $y = 48.8$ (corresponding to their peak position, see Fig. 19), for the norm approximations E_1 (a), E_2 (b), and $E_3^{\delta^*}$ (c). The solutions are obtained for $Ri = 10^{-2}$, $Re = 500$, $Pr = 0.7$, $\alpha = 0.35$, $\beta = 0.75$, and $L_y = 100$.

notice that the first peak is not affected at all by the different norm approximations, as shown in Fig. 17, since the ϕ parameter mostly varies at the free stream, whereas the initial short-time optimal perturbations are localized within the boundary layer.

An increase of the transient growth in a stratified channel flow with respect to the unstratified case was reported in Ref. [6], for transient growth optimizations performed with an energy norm having $\phi = 1$. Also in that case the optimal perturbation was characterized by spanwise-independent rolls, instead of streamwise vortices found at $Pr = 0$. In Ref. [40], an amplification mechanism has been studied in which density perturbations advected in a shear flow are able to force the wall-normal velocity perturbations, inducing an algebraic growth in nonstratified and weakly (stably) stratified shear flows, and a sublinear growth in strongly stratified ones. Similarly to what observed in the present case, the authors found that the larger the initial density (or temperature) perturbation, the larger the kinetic energy growth, and the longer the amplification is sustained for. The present long-time energy growth mechanism, which is indeed optimal for some of the considered approximations of the energy, appears to be the same as that reported in [40].

Although in both cases the reported energy growth is nonoptimal in terms of the total (kinetic plus potential) energy, it can be still relevant for atmospheric boundary layer flows, in which strong temperature fluctuations can be induced by the presence of buildings or due to wind changes. Growing in time and being amplified by several orders of magnitude, such perturbations may have crucial implications for stirring up the flow toward turbulent conditions and/or generating bursts.

When nonlinearity sets in, these structures might become self-sustained, in the same way as linear optimal perturbations such as streaks are observed in turbulent flows [41,42]. Notably, coherent structures similar to the long-time optimal perturbations found here are reported in Ref. [8] in the centerline region of stably stratified turbulent channel flow, and as discussed by the authors, they match the main features found by kinetic energy optimization in the same flow case [43]. It is thus possible that in turbulent conditions, in which the fluctuations with respect to the mean flow pervade the flow at all scales, this mechanism might be triggered.

IV. CONCLUSIONS

This paper investigates the modal and nonmodal linear stability of a stably stratified Blasius boundary layer flow. The base flow is composed of a velocity and a thermal Blasius boundary layer whose thicknesses scale with the cubic root of the Prandtl number. The spatial linear stability of such a flow is investigated for different Richardson, Reynolds, and Prandtl numbers. While increasing the Richardson number stabilizes the flow, pushing the critical Reynolds Re_c to values greater than 2000 for $Ri > 10^{-2}$, a more complex behavior is found when changing the Prandtl number. In fact, increasing this parameter up to $Pr = 7$ stabilizes the flow for $Re_c < 1200$; a further increase of Pr is found to destabilize the flow, leading to a drop of the critical Reynolds number to values

even lower than that of the nonstratified case. In fact, an increase of the Prandtl number usually translates into a stabilization of the flow since the thermal diffusivity of the flow increases with respect to viscosity. However, the concurrent weakening of the diffusion term in the temperature may tend to facilitate the growth of temperature perturbations. Thus, for certain values of Re and Pr, the destabilizing effect of the reduced thermal diffusion can overcome the usually encountered stabilizing effect, as observed in the present case. Moreover, the Prandtl number influences also the wall-normal distribution of the unstable eigenvector profiles, whose peak values move toward the wall when Pr increases, due to the variation of the wall-normal position of the critical layer with the Prandtl number.

The nonmodal linear stability of the stably stratified boundary layer flow is then investigated using a direct-adjoint looping procedure aiming at optimizing an opportunely weighted sum of the kinetic and potential energies. In the present case of the Blasius boundary layer, the potential energy value has a peculiar divergent behavior in the free-stream flow region since the derivative of the base-temperature (density) profile with respect to the y coordinate is zero. Therefore, we have tried to overcome this singularity using different approximations of the norm, showing to which extent the choice of the potential energy terms approximation influences the study of the transient growth for the case of the Blasius boundary layer. Thus, three approximations of the energy have been considered as objective functions of the optimization procedure: (i) E_1, considering only the contribution of the kinetic energy; (ii) E_2, in which the derivative of the base-flow temperature field is approximated by a constant value close to the average value measured within the boundary layer; (iii) E_3, in which the variation of the stratification strength with height is taken into account and the singularity is overcome by taking the exact base-flow temperature derivative up to a given wall-normal position $\bar{y}$, whereas, for $y > \bar{y}$, it is fixed to a (small, although nonzero) constant value. The energy optimization is carried out at first for short [$O(10)$] target times, recovering the same results for all the approximations of the norm. In all cases, we have found that increasing the Richardson number, the optimal energy gain and the time at which it is obtained decrease, whereas the optimal streamwise wave number considerably departs from zero (i.e., its optimal value in the nonstratified case). Moreover, increasing the Richardson number, the dependence of the energy growth on the Reynolds number evolves from a quadratic to a linear behavior, whereas the optimal time, which varies linearly with Re in the nonstratified case, remains constant no matter the Reynolds number. This suggests that the optimal energy growth mechanism in the stratified case is not merely the lift-up one, even if elongated (although inclined) high-streamwise-momentum flow structures are found at optimal time. A closer inspection of the optimal perturbations shows spanwise vorticity structures inclined against the mean flow direction, which tilt in the streamwise direction in time, increasing their energy due to the Orr mechanism. Following the time variation of the different energy-production terms, we notice that, as Ri increases, the lift-up related production term peaks earlier in time, to avoid the counterbalancing effect of the buoyancy production term. Thus, the optimal timescale of the lift-up mechanism collapses with that of the Orr one, leading to an oblique optimal perturbation which exploits both mechanisms for amplifying its energy. Although large amplification of three-dimensional oblique wave perturbations is achieved in many plane shear flows for very short times [38], it is found to be the overall optimal only for a very few cases, such as the unbounded infinite-shear flow [38] and a shear flow with free surface at low Froude number [39]. In most of the shear flows, such as the mixing layer [13] and many wall-bounded shear flows such as the Couette, the plane Poiseuille, and the boundary layer flow, of interest here, this synergistic mechanism is overcome by the energy growth of two-dimensional perturbations at larger timescales (Kelvin-Helmoltz–type perturbations in the former case, streaks in the latter). In the present case, stable stratification damps the lift-up mechanism and produces a reduction of its optimal timescale in order to avoid a too strong growth of the (negative) buoyancy production term, leading to a three-dimensional, oblique optimal structure for sufficiently high Richardson numbers.

A further analysis of the different energy-production terms shows that another transient amplification mechanism is active, directly linked to the increase of the buoyancy flux production term, by the coupling of wall-normal velocity and thermal perturbations of the same sign. This

amplification mechanism is indeed observed for long $[O(1000)]$ target times, leading to a perturbation characterized by counter-rotating vortices constituted of negative wall-normal velocities pushing negative temperature perturbations toward the boundary layer region, and positive wall-normal velocity disturbances lifting up positive temperature fluctuations. This mechanism appears to be optimal only for some approximations of the total-energy norm, in which the potential energy is neglected or the variation of the stratification strength with height is roughly approximated. When the variation of stratification with height is correctly taken into account, the long-time energy peak disappears since the relative weight of temperature perturbations, placed at the free stream with respect to velocity ones, becomes huge. Although the reported energy growth is not optimal in terms of the total energy, it can be still relevant for atmospheric boundary layer flows, in which strong temperature fluctuations can be induced by the presence of buildings or due to wind changes. Growing in time and being amplified by several orders of magnitude, such perturbations may have crucial implications for stirring up the flow toward turbulent conditions and/or generating bursts. Notably, coherent structures similar to the long-time optimal perturbations found here are reported in Ref. [8] in the centerline region of stably stratified turbulent channel flow, and as discussed by the authors, they match the main features found by kinetic energy optimization in the same flow case [43]. It is thus possible that in turbulent conditions, in which the fluctuations with respect to
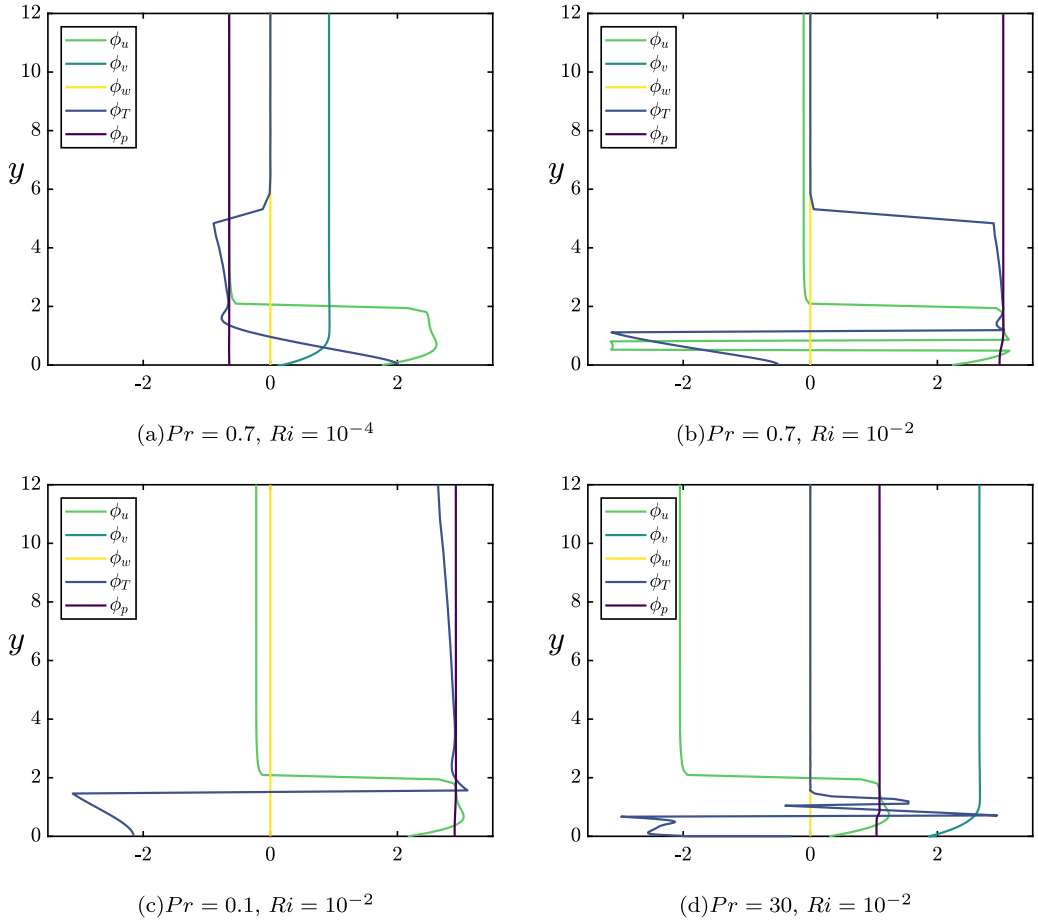

FIG. 22. Phase of the five components of the unstable eigenvectors for the stratified Blasius flow at critical conditions (indicated in Table I) for different Richardson and Prandtl numbers.

the mean flow pervade the flow at all scales, this mechanism would be triggered. Future works will aim at investigating such a possibility in turbulent boundary layer flows with stable stratification. In some other cases in which a direct measure of potential energy is not possible, other measures of optimality will need to be needed, such as the kinetic energy, for which the present mechanism is indeed optimal. This indicates that these perturbations may be indeed relevant for the flow dynamics in the transitional and turbulent regimes.

This paper has shown how the presence of a stable stratification in a boundary layer flow can considerably modify the asymptotic stability of the flow, its energy amplification mechanisms, timescales, and their dependence on the Reynolds number, as well as triggering different energy growth mechanisms. The optimally growing perturbations are likely to represent the main features of the coherent structures that characterize the turbulent flow, in the same way as optimally growing streaky structures populate turbulent shear flows. Future work will aim to extend this analysis to the case of a turbulent boundary layer in the presence of different stable stratifications (from weak to strong). This will allow one to unravel which coherent structures may be the most representative of the dynamics of an atmospheric boundary layer flow.
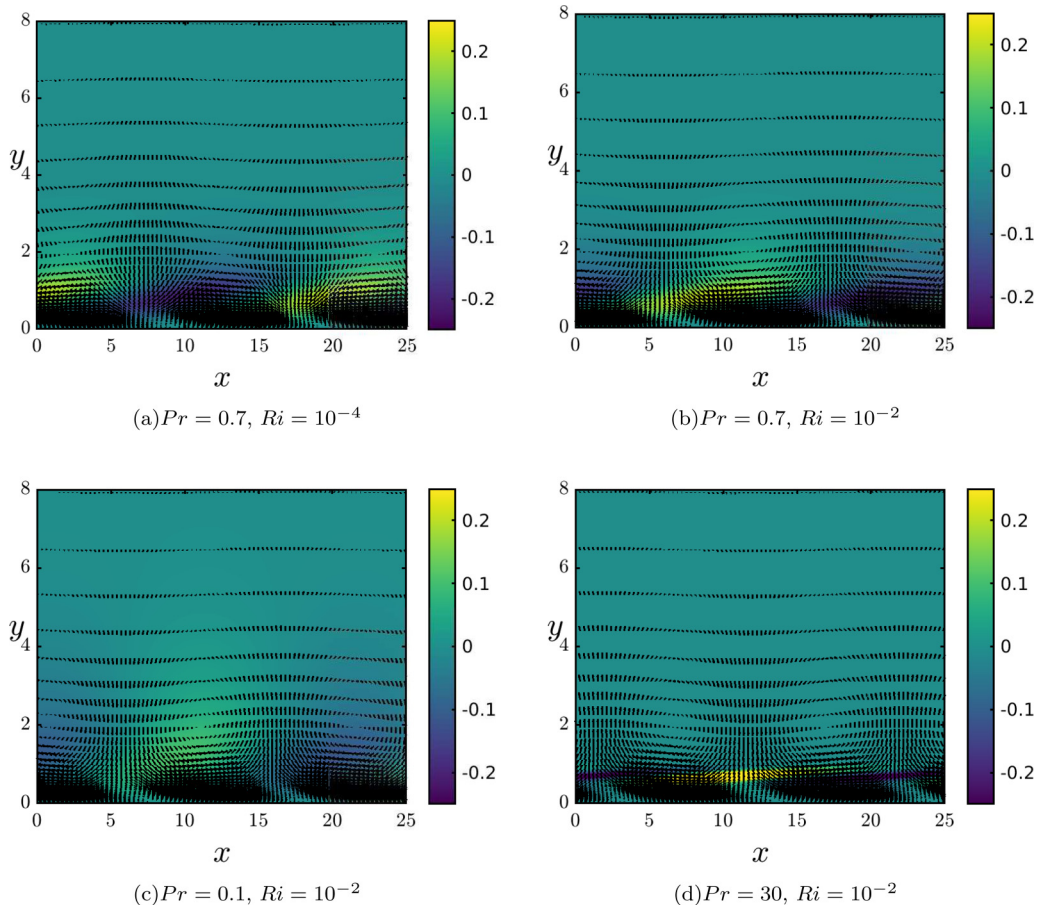

FIG. 23. Spatial structure of the unstable eigenvectors for the stratified Blasius flow at critical conditions (indicated in Table I) for different Richardson and Prandtl numbers: contours of the temperature component and vectors of the velocity component on a x-y plane.

APPENDIX

In this Appendix we show the phase of the five components of the unstable eigenvectors for the stratified Blasius flow at critical conditions (indicated in Table I) for different Richardson and Prandtl numbers. In Fig. 22, the phase evolution is observed in the wall-normal direction for the u, v, and T components, which are directly involved in the instability mechanisms previously discussed. In particular, for all the considered values of Ri and Pr, the phase of u and v has almost the same wall-normal distribution typical of TS waves. Whereas, the temperature component phase appears to be much more affected by the amount of stratification, showing a rather different distribution in the wall-normal direction when Ri and Pr change. This results into a different spatial structure of the temperature component, as shown in Fig. 23. In particular, the Prandtl number appears to have a strong effect onto the wall-normal distribution and relative amplitude of T, leading to weaker but more extended patches of temperature for lower Pr values, whereas stronger and more localized temperature variations are observed for higher values of Pr (compare the last two frames of Fig. 23). Instead, as anticipated, the spatial structure of the velocity components barely changes with Ri and Pr.

[1] T. Asai, Stability of a plane parallel flow with variable vertical shear and unstable stratification, J. Meteorol. Soc. Jpn. **48**, 129 (1970).

[2] K. S. Gage and W. H. Reid, The stability of thermally stratified plane poiseuille flow, J. Fluid Mech. **33**, 21 (1968).

[3] J. John Soundar Jerome, J.-M. Chomaz, and P. Huerre, Transient growth in Rayleigh-Bénard-Poiseuille/Couette convection, Phys. Fluids **24**, 044103 (2012).

[4] G. Facchini, B. Favier, P. Le Gal, M. Wang, and M. Le Bars, The linear instability of the stratified plane couette flow, J. Fluid Mech. **853**, 205 (2018).

[5] D. Biau and A. Bottaro, The effect of stable thermal stratification on shear flow stability, Phys. Fluids **16**, 4742 (2004).

[6] A. Sameen and R. Govindarajan, The effect of wall heating on instability of channel flow, J. Fluid Mech. **577**, 417 (2007).

[7] C. Yáñez Vico, Transient development of perturbations in a stratified turbulent shear flow. Ph.D. thesis, M.S. thesis, Universidad Politécnica de Madrid and University of Karlsruhe, 2008. http://oa.upm.es/1446/1/PFC_CARLOS_YANEZ_VICO.pdf.

[8] M. García-Villalba and J. C. del Álamo, Turbulence modification by stable stratification in channel flow, Phys. Fluids **23**, 045104 (2011).

[9] R. V. K. Chakravarthy, L. Lesshafft, and P. Huerre, Local linear stability of laminar axisymmetric plumes, J. Fluid Mech. **780**, 344 (2015).

[10] R. V. K. Chakravarthy, L. Lesshafft, and P. Huerre, Global stability of buoyant jets and plumes, J. Fluid Mech. **835**, 654 (2018).

[11] C. P. Caulfield and W. R. Peltier, The anatomy of the mixing transition in homogeneous and stratified free shear layers., J. Fluid Mech. **413**, 1 (2000).

[12] A. K. Kaminski, C. P. Caulfield, and J. R. Taylor, Transient growth in strongly stratified shear layers, J. Fluid Mech. **758**, R4 (2014).

[13] C. Arratia, C. P. Caulfield, and J.-M. Chomaz, Transient perturbation growth in time-dependent mixing layers, J. Fluid Mech. **717**, 90 (2013).

[14] P. A. Davis and W. R. Peltier, Resonant parallel shear instability in the stably stratified planetary boundary layer, J. Atmos. Sci. **33**, 1287 (1976).

[15] G. Chimonas, On internal gravity waves associated with the stable boundary layer, Boundary-Layer Meteorol. **102**, 139 (2002).

[16] J. Candelier, S. Le Dizès, and C. Millet, Inviscid instability of a stably stratified compressible boundary layer on an inclined surface, J. Fluid Mech. **694**, 524 (2012).

[17] X. Wu and J. Zhang, Instability of a stratified boundary layer and its coupling with internal gravity waves. part 1. linear and nonlinear instabilities, J. Fluid Mech. **595**, 379 (2008).

[18] J. Chen, Y. Bai, and S. Le Dizès, Instability of a boundary layer flow on a vertical wall in a stably stratified fluid, J. Fluid Mech. **795**, 262 (2016).

[19] P. J. Schmid and D. S. Henningson, *Stability and Transition in Shear Flows* (Springer, New York, 2012), Vol. 142.

[20] D. Holliday and M. E. Mcintyre, On potential energy density in an incompressible, stratified fluid, J. Fluid Mech. **107**, 221 (1981).

[21] T. G. Shepherd, A unified theory of available potential energy, Atmos.-Ocean **31**, 1 (1993).

[22] R. Tailleux, Available potential energy and exergy in stratified fluids, Annu. Rev. Fluid Mech. **45**, 35 (2013).

[23] N. Reina and L. Mahrt, A study of intermittent turbulence with cases-99 tower measurments, Boundary-Layer Meteorol. **114**, 367 (2005).

[24] H. Schlichting, *Boundary Layer Theory* (Springer, Berlin, 1979).

[25] S. Cherubini, P. De Palma, J. C. Robinet, and A. Bottaro, Optimal wave packets in a boundary layer and initial phases of a turbulent spot, J. Fluid Mech. **656**, 231 (2010).

[26] A. Monokrousos, A. Bottaro, L. Brandt, A. Di Vita, and D. S. Henningson, Non-Equilibrium Thermodynamics and the Optimal Path to Turbulence in Shear Flows, Phys. Rev. Lett. **106**, 134502 (2011).

[27] D. P. G. Foures, C. P. Caulfield, and P. Schmid, Localization of flow structures using infinity-norm optimization, J. Fluid Mech. **729**, 672 (2013).

[28] D. P. G. Foures, C. P. Caulfield, and P. J. Schmid, Variational framework for flow optimization using seminorm constraints, Phys. Rev. E **86**, 026306 (2012).

[29] S. Cherubini, P. De Palma, J. C. Robinet, and A. Bottaro, The minimal seed of turbulent transition in a boundary layer, J. Fluid Mech. **689**, 221 (2011).

[30] D. Barkley, H. M. Blackburn, and S. J. Sherwin, Direct optimal growth analysis for timesteppers, Int. J. Numer. Methods Fluids **57**, 1435 (2008).

[31] P. J. Schmid, Linear stability theory and bypass transition in shear flows, Phys. Plasmas **7**, 1788 (2000).

[32] M. T. Landahl, A note on an algebraic instability of inviscid parallel shear flows, J. Fluid Mech. **98**, 243 (1980).

[33] A. K. Kaminski, C. P. Caulfield, and J. R. Taylor, Nonlinear evolution of linear optimal perturbations of strongly stratified shear layers, J. Fluid Mech. **825**, 213 (2017).

[34] K. M. Butler and B. F. Farrell, Three-dimensional optimal perturbations in viscous shear flow, Phys. Fluids A **4**, 1637 (1992).

[35] P. Luchini, Reynolds-number-independent instability of the boundary layer over a flat surface: Optimal perturbations, J. Fluid Mech. **404**, 289 (2000).

[36] L. Brandt, The lift-up effect: The linear mechanism behind transition and turbulence in shear flows, Eur. J. Mech. B **47**, 80 (2014).

[37] William M'F. Orr, The Stability or Instability of the Steady Motions of a Perfect Liquid and of a Viscous Liquid. Part I: A Perfect Liquid, Proc. R. Irish. Acad. **27**, 9 (1907).

[38] B. F. Farrell and P. J. Ioannou, Optimal excitation of three-dimensional perturbations in viscous constant shear flow, Phys. Fluids A **5**, 1390 (1993).

[39] C. Mallios and N. A. Bakas, Generalized stability of a shear flow with a free surface with respect to three-dimensional perturbations, Phys. Rev. Fluids **2**, 023901 (2017).

[40] S. Jose, A. Roy, R. Bale, and R. Govindarajan, Analytical solutions for algebraic growth of disturbances in a stably stratified shear flow, Proc. R. Soc. London, Ser. A **471**, 20150267 (2015).

[41] C. Cossu, G. Pujals, and S. Depardon, Optimal transient growth and very large-scale structures in turbulent boundary layers, J. Fluid Mech. **619**, 79 (2009).

[42] M. Farano, S. Cherubini, J.-C. Robinet, and P. De Palma, Optimal bursts in turbulent channel flow, J. Fluid Mech. **817**, 35 (2017).

[43] J. C. Del Alamo, C. Yanez, and M. Garcia-Villalba, Linear analysis of transient growth in stably-stratified, turbulent channel flow, Bull. Am. Phys. Soc. **64**, A7.007 (2011).